



JET CRACKLE

Jonathan Freund
UNIVERSITY OF ILLINOIS CHAMPAIGN

06/23/2015
Final Report

DISTRIBUTION A: Distribution approved for public release.

Air Force Research Laboratory
AF Office Of Scientific Research (AFOSR)/ RTE
Arlington, Virginia 22203
Air Force Materiel Command

REPORT DOCUMENTATION PAGE					Form Approved OMB No. 0704-0188	
<p>The public reporting burden for this collection of information is estimated to average 1 hour per response, including the time for reviewing instructions, searching existing data sources, gathering and maintaining the data needed, and completing and reviewing the collection of information. Send comments regarding this burden estimate or any other aspect of this collection of information, including suggestions for reducing the burden, to the Department of Defense, Executive Service Directorate (0704-0188). Respondents should be aware that notwithstanding any other provision of law, no person shall be subject to any penalty for failing to comply with a collection of information if it does not display a currently valid OMB control number.</p> <p>PLEASE DO NOT RETURN YOUR FORM TO THE ABOVE ORGANIZATION.</p>						
1. REPORT DATE (DD-MM-YYYY) 5/10/2015		2. REPORT TYPE FINAL			3. DATES COVERED (From - To) 08/15/2010 to 02/14/2015	
4. TITLE AND SUBTITLE JET CRACKLE				5a. CONTRACT NUMBER FA9550-10-1-0432		
				5b. GRANT NUMBER		
				5c. PROGRAM ELEMENT NUMBER		
6. AUTHOR(S) JONATHAN B. FREUND DAVID A. BUCHTA				5d. PROJECT NUMBER		
				5e. TASK NUMBER		
				5f. WORK UNIT NUMBER		
7. PERFORMING ORGANIZATION NAME(S) AND ADDRESS(ES) University of Illinois at Urbana- Champaign Urbana, IL 61801					8. PERFORMING ORGANIZATION REPORT NUMBER	
9. SPONSORING/MONITORING AGENCY NAME(S) AND ADDRESS(ES) Air Force Office of Scientific Research 875 North Randolph Street, Suite 325, Room 3112, Arlington, VA., 22203-1768					10. SPONSOR/MONITOR'S ACRONYM(S) AFOSR	
					11. SPONSOR/MONITOR'S REPORT NUMBER(S)	
12. DISTRIBUTION/AVAILABILITY STATEMENT DISTRIBUTION A						
13. SUPPLEMENTARY NOTES						
14. ABSTRACT Fighter jets and other aircraft with high specific thrust engines can make a particularly intense type of noise that has come to be called crackle. It is unmistakably different than lower speed jet noise. Its frequency content, extreme intensity, and sporadic character make it particularly annoying and potentially injurious to insufficiently protected hearing. We have complete a set of detailed direct numerical simulations of free shear flows to investigate turbulence as a source of jet crackle. This report includes (1) detailed documentation of these simulations, (2) their verification and validation, (3) and several post-processing investigation the underlying mechanics of jet crackle, including detailed quantification of the near acoustic field, analysis of statistical metrics of jet crackle, analysis of sound-field nonlinear effects, and the relation of crackle to the linear instability modes supported by free shear flows. This is the first-ever such detailed investigation of these mechanisms.						
15. SUBJECT TERMS Jet Noise, Turbulence, High-speed flows						
16. SECURITY CLASSIFICATION OF:			17. LIMITATION OF ABSTRACT	18. NUMBER OF PAGES	19a. NAME OF RESPONSIBLE PERSON	
a. REPORT	b. ABSTRACT	c. THIS PAGE			Jonathan B Freund	
U	U	U	UU	44	19b. TELEPHONE NUMBER (Include area code) 217-244-7729	

Reset

INSTRUCTIONS FOR COMPLETING SF 298

1. REPORT DATE. Full publication date, including day, month, if available. Must cite at least the year and be Year 2000 compliant, e.g. 30-06-1998; xx-06-1998; xx-xx-1998.

2. REPORT TYPE. State the type of report, such as final, technical, interim, memorandum, master's thesis, progress, quarterly, research, special, group study, etc.

3. DATES COVERED. Indicate the time during which the work was performed and the report was written, e.g., Jun 1997 - Jun 1998; 1-10 Jun 1996; May - Nov 1998; Nov 1998.

4. TITLE. Enter title and subtitle with volume number and part number, if applicable. On classified documents, enter the title classification in parentheses.

5a. CONTRACT NUMBER. Enter all contract numbers as they appear in the report, e.g. F33615-86-C-5169.

5b. GRANT NUMBER. Enter all grant numbers as they appear in the report, e.g. AFOSR-82-1234.

5c. PROGRAM ELEMENT NUMBER. Enter all program element numbers as they appear in the report, e.g. 61101A.

5d. PROJECT NUMBER. Enter all project numbers as they appear in the report, e.g. 1F665702D1257; ILIR.

5e. TASK NUMBER. Enter all task numbers as they appear in the report, e.g. 05; RF0330201; T4112.

5f. WORK UNIT NUMBER. Enter all work unit numbers as they appear in the report, e.g. 001; AFAPL30480105.

6. AUTHOR(S). Enter name(s) of person(s) responsible for writing the report, performing the research, or credited with the content of the report. The form of entry is the last name, first name, middle initial, and additional qualifiers separated by commas, e.g. Smith, Richard, J, Jr.

7. PERFORMING ORGANIZATION NAME(S) AND ADDRESS(ES). Self-explanatory.

8. PERFORMING ORGANIZATION REPORT NUMBER. Enter all unique alphanumeric report numbers assigned by the performing organization, e.g. BRL-1234; AFWL-TR-85-4017-Vol-21-PT-2.

9. SPONSORING/MONITORING AGENCY NAME(S) AND ADDRESS(ES). Enter the name and address of the organization(s) financially responsible for and monitoring the work.

10. SPONSOR/MONITOR'S ACRONYM(S). Enter, if available, e.g. BRL, ARDEC, NADC.

11. SPONSOR/MONITOR'S REPORT NUMBER(S). Enter report number as assigned by the sponsoring/monitoring agency, if available, e.g. BRL-TR-829; -215.

12. DISTRIBUTION/AVAILABILITY STATEMENT. Use agency-mandated availability statements to indicate the public availability or distribution limitations of the report. If additional limitations/ restrictions or special markings are indicated, follow agency authorization procedures, e.g. RD/FRD, PROPIN, ITAR, etc. Include copyright information.

13. SUPPLEMENTARY NOTES. Enter information not included elsewhere such as: prepared in cooperation with; translation of; report supersedes; old edition number, etc.

14. ABSTRACT. A brief (approximately 200 words) factual summary of the most significant information.

15. SUBJECT TERMS. Key words or phrases identifying major concepts in the report.

16. SECURITY CLASSIFICATION. Enter security classification in accordance with security classification regulations, e.g. U, C, S, etc. If this form contains classified information, stamp classification level on the top and bottom of this page.

17. LIMITATION OF ABSTRACT. This block must be completed to assign a distribution limitation to the abstract. Enter UU (Unclassified Unlimited) or SAR (Same as Report). An entry in this block is necessary if the abstract is to be limited.

REPORT DOCUMENTATION PAGE					<i>Form Approved</i> OMB No. 0704-0188	
<p>The public reporting burden for this collection of information is estimated to average 1 hour per response, including the time for reviewing instructions, searching existing data sources, gathering and maintaining the data needed, and completing and reviewing the collection of information. Send comments regarding this burden estimate or any other aspect of this collection of information, including suggestions for reducing the burden, to the Department of Defense, Executive Service Directorate (0704-0188). Respondents should be aware that notwithstanding any other provision of law, no person shall be subject to any penalty for failing to comply with a collection of information if it does not display a currently valid OMB control number.</p> <p>PLEASE DO NOT RETURN YOUR FORM TO THE ABOVE ORGANIZATION.</p>						
1. REPORT DATE (DD-MM-YYYY)		2. REPORT TYPE			3. DATES COVERED (From - To)	
4. TITLE AND SUBTITLE				5a. CONTRACT NUMBER		
				5b. GRANT NUMBER		
				5c. PROGRAM ELEMENT NUMBER		
6. AUTHOR(S)				5d. PROJECT NUMBER		
				5e. TASK NUMBER		
				5f. WORK UNIT NUMBER		
7. PERFORMING ORGANIZATION NAME(S) AND ADDRESS(ES)					8. PERFORMING ORGANIZATION REPORT NUMBER	
9. SPONSORING/MONITORING AGENCY NAME(S) AND ADDRESS(ES)					10. SPONSOR/MONITOR'S ACRONYM(S)	
					11. SPONSOR/MONITOR'S REPORT NUMBER(S)	
12. DISTRIBUTION/AVAILABILITY STATEMENT						
13. SUPPLEMENTARY NOTES						
14. ABSTRACT						
15. SUBJECT TERMS						
16. SECURITY CLASSIFICATION OF:			17. LIMITATION OF ABSTRACT	18. NUMBER OF PAGES	19a. NAME OF RESPONSIBLE PERSON	
a. REPORT	b. ABSTRACT	c. THIS PAGE			19b. TELEPHONE NUMBER (Include area code)	

INSTRUCTIONS FOR COMPLETING SF 298

1. REPORT DATE. Full publication date, including day, month, if available. Must cite at least the year and be Year 2000 compliant, e.g. 30-06-1998; xx-06-1998; xx-xx-1998.

2. REPORT TYPE. State the type of report, such as final, technical, interim, memorandum, master's thesis, progress, quarterly, research, special, group study, etc.

3. DATES COVERED. Indicate the time during which the work was performed and the report was written, e.g., Jun 1997 - Jun 1998; 1-10 Jun 1996; May - Nov 1998; Nov 1998.

4. TITLE. Enter title and subtitle with volume number and part number, if applicable. On classified documents, enter the title classification in parentheses.

5a. CONTRACT NUMBER. Enter all contract numbers as they appear in the report, e.g. F33615-86-C-5169.

5b. GRANT NUMBER. Enter all grant numbers as they appear in the report, e.g. AFOSR-82-1234.

5c. PROGRAM ELEMENT NUMBER. Enter all program element numbers as they appear in the report, e.g. 61101A.

5d. PROJECT NUMBER. Enter all project numbers as they appear in the report, e.g. 1F665702D1257; ILIR.

5e. TASK NUMBER. Enter all task numbers as they appear in the report, e.g. 05; RF0330201; T4112.

5f. WORK UNIT NUMBER. Enter all work unit numbers as they appear in the report, e.g. 001; AFAPL30480105.

6. AUTHOR(S). Enter name(s) of person(s) responsible for writing the report, performing the research, or credited with the content of the report. The form of entry is the last name, first name, middle initial, and additional qualifiers separated by commas, e.g. Smith, Richard, J, Jr.

7. PERFORMING ORGANIZATION NAME(S) AND ADDRESS(ES). Self-explanatory.

8. PERFORMING ORGANIZATION REPORT NUMBER. Enter all unique alphanumeric report numbers assigned by the performing organization, e.g. BRL-1234; AFWL-TR-85-4017-Vol-21-PT-2.

9. SPONSORING/MONITORING AGENCY NAME(S) AND ADDRESS(ES). Enter the name and address of the organization(s) financially responsible for and monitoring the work.

10. SPONSOR/MONITOR'S ACRONYM(S). Enter, if available, e.g. BRL, ARDEC, NADC.

11. SPONSOR/MONITOR'S REPORT NUMBER(S). Enter report number as assigned by the sponsoring/monitoring agency, if available, e.g. BRL-TR-829; -215.

12. DISTRIBUTION/AVAILABILITY STATEMENT. Use agency-mandated availability statements to indicate the public availability or distribution limitations of the report. If additional limitations/ restrictions or special markings are indicated, follow agency authorization procedures, e.g. RD/FRD, PROPIN, ITAR, etc. Include copyright information.

13. SUPPLEMENTARY NOTES. Enter information not included elsewhere such as: prepared in cooperation with; translation of; report supersedes; old edition number, etc.

14. ABSTRACT. A brief (approximately 200 words) factual summary of the most significant information.

15. SUBJECT TERMS. Key words or phrases identifying major concepts in the report.

16. SECURITY CLASSIFICATION. Enter security classification in accordance with security classification regulations, e.g. U, C, S, etc. If this form contains classified information, stamp classification level on the top and bottom of this page.

17. LIMITATION OF ABSTRACT. This block must be completed to assign a distribution limitation to the abstract. Enter UU (Unclassified Unlimited) or SAR (Same as Report). An entry in this block is necessary if the abstract is to be limited.

FINAL REPORT:
JET CRACKLE
AFOSR GRANT #FA9550-10-1-0432

JONATHAN B. FREUND
DAVID A. BUCHTA

*Department of Mechanical Science & Engineering
University of Illinois at Urbana- Champaign Urbana, IL 61801*

Contents

1	Summary	5
2	Introduction	5
2.1	Background	5
2.2	Objectives and outline	7
3	Simulation details	8
3.1	Configuration	8
3.2	Numerical methods	9
4	Results	11
4.1	Turbulence statistics	11
4.2	Near-field acoustics	13
4.3	Near-field nonlinearity	14
5	Pressure variance and skewness budget	18
5.1	Derivation	18
5.2	Results	25
6	Conclusions	26
7	Personnel supported during duration of grant	26
8	AFOSR point of contact	27
9	Publications	27
10	Acknowledgment/disclaimer	28
A	Flow equations	29
B	Numerics	31
B.1	Discrete Fourier method	31
B.2	Finite difference first derivative	32
B.3	Finite difference second derivative	34
B.4	Selective high-wave number filtering	36
C	Reynolds number effect	38
D	Instability modes of inviscid parallel temporal shear layers	38

Abstract

Fighter jets and other aircraft with high specific thrust engines can make a particularly intense type of noise that has come to be called crackle. Its rough, sporadic character is sometimes likened to super-loud paper tearing or the sharp staccato of water drops added to hot oil. It is unmistakably different than lower speed jet noise. Its frequency content, extreme intensity, and sporadic character make it particularly annoying and potentially injurious to insufficiently protected hearing. Observations suggest that it consists of series of intense shock-like sound waves, which arrive intermittently in groups. Between these shock groups a less intense but still loud standard jet noise is heard. The steepened shock-like character is suggestive of nonlinear development, but to what degree they attain this character at generation versus nonlinear steepening during propagation is unclear. There is evidence that both are key factors in crackle. It is also unclear whether the intermittency of crackle is due to the changing character of the turbulence or if it is a stochastic propagation effect.

We have complete a set of detailed direct numerical simulations of free shear flows to investigate turbulence as a source of jet crackle. This report includes (1) detailed documentation of these simulations, (2) their verification and validation, (3) and several post-processing investigation the underlying mechanics of jet crackle, including detailed quantification of the near acoustic field, analysis of statistical metrics of jet crackle, analysis of sound-field nonlinear effects, and the relation of crackle to the linear instability modes supported by free shear flows. This is the first-ever such detailed investigation of these mechanisms.

1 Summary

The summary of our accomplishments of this funding period are:

- We completed a detailed study of the turbulence and radiated sound of high-speed turbulent shear layers for Mach numbers, $M = 0.9, 1.5, 2.5$, and 3.5 . The results indicate that for $M \gtrsim 2.5$ crackle noise correlated to pressure skewness $S_k(p') \gtrsim 0.4$ is present in the very near acoustic field. This was the first such detailed DNS investigation of turbulence as a source of crackle.
- We confirmed that these flows have broad-banded, realistic turbulence and that low-order statistics match well with previous simulation and their planar shear layer experimental counterpart.
- Detailed analysis of the near-field acoustics shows weak shock-like waves undergo nonlinear interactions during sound propagation leading to elevated skewness in the very near field. After that, they propagate with little additional nonlinear distortion.
- We completed a higher-Reynolds number simulation for $M = 2.5$ at twice the grid resolution. The results show that crackle is independent of Reynolds number, for the Reynolds number range considered.
- An analysis using linear stability theory of a parallel shear flow was completed. It is clear that for $M \gtrsim 1.2$ ($M_c \gtrsim 0.6$) the flow becomes more three-dimensional which is reflected in the turbulence statistics.
- A formulation of the statistical skewness budget was evaluated in the near acoustic field. The results indicate statistical skewness originates near or at the turbulent source. The effect of heat conduction and viscosity which would serve to decrease statistical skewness is nearly balanced by other acoustic contributions. This suggests the footprint of elevated skewness arises near the turbulence and propagates nearly unchanged over distances considered in the DNS.

2 Introduction

2.1 Background

Military aircraft and other jet engines operating with high-specific thrust have been observed to radiate a particularly intense and distinct sound that has become known as ‘crackle’. Crackle has been described

as a ‘startling staccato of cracks and bangs’ (Ffowcs Williams *et al.*, 1975) and, although a very annoying aspect of jet noise when observed from a distance, this distinct sound can cause aural injury for personnel working in close proximity. Reducing or eliminating crackle from the overall jet noise would reduce annoyance, improve environmental noise levels near airbases, and decrease the potential for injury.

Crackle has been extensively documented after it was first reported as a distinct phenomenon by Ffowcs Williams *et al.* (1975) for supersonic full-scale engines and lab-scale jets. Although crackle is an extremely intense sound, it is the intermittency of crackle that makes it particularly annoying (Ffowcs Williams *et al.*, 1975). At seemingly random times, crackle lasts between 0.1 and 1 seconds at 1 to 2 second intervals (Ffowcs Williams *et al.*, 1975). During this period, strong shock-like compressions are observed at a frequency of 10^{-2} seconds. The time trace of acoustic pressure during a crackle event reveals a peculiar feature—strong, steepened compressions (lasting 1 millisecond) followed by longer weaker expansions (lasting 2 to 3 milliseconds) with the expansion amplitude about $\frac{1}{4}$ the compression peak. The authors noticed that the statistical skewness of acoustic pressure would quantify the amplitude asymmetry between the sharp, intense peaks and rounded, weaker valleys in the sound signal. Correlating the perception of crackle with statistical skewness,

$$S_k(p') = \frac{\langle (p')^3 \rangle}{\langle (p')^2 \rangle^{3/2}}, \quad (1)$$

It was observed that sound with $S_k(p') \gtrsim 0.4$ would be noticeably crackling. Though not a rigorous definition, statistical skewness is a suitable metric for correlating to the perception of crackle (Ffowcs Williams *et al.*, 1975; Krothapalli *et al.*, 2000; Petitjean & McLaughlin, 2003; Petitjean *et al.*, 2005). Gee *et al.* (2007) suggests that the skewness of the time derivative of pressure is a suitable metric for quantifying sharp changes in the pressure signal, which are also known to occur in crackle noise. Other metrics such as pressure spectra are insensitive to detecting the presence of crackle (Ffowcs Williams *et al.*, 1975) in part because of its intermittency: crackle events occurring in about 5% of the acoustic signal (Krothapalli *et al.*, 2000).

Crackle levels depend on jet operating conditions. $S_k(p')$ is known to increase with increasing flow velocity (Ffowcs Williams *et al.*, 1975; Szewczyk, 1978; Krothapalli *et al.*, 2000; Petitjean & McLaughlin, 2003; Petitjean *et al.*, 2005; Gee *et al.*, 2013) and crackle is apparent when the jet velocity is high enough that turbulent eddies in the shear layer move supersonically relative to the ambient free stream (Krothapalli *et al.*, 2003). Initially thought to be insensitive to jet temperature (Ffowcs Williams *et al.*, 1975; Szewczyk, 1978), within the temperature range tested, crackle levels do correlate with higher temperature ratios (Krothapalli *et al.*, 2000; Petitjean & McLaughlin, 2003). The frequency of the sporadic crackle events also increases with increasing jet velocity and temperature. Crackle does not seem to be correlated to the presence of internal shock-cells from imperfect expansion (Ffowcs Williams *et al.*, 1975; Szewczyk, 1978; Krothapalli *et al.*, 2000) nor to rough combustion processes present in full-scale engine tests (Ffowcs Williams *et al.*, 1975). High skewness levels have been correlated to angles near the expected Mach angle (Ffowcs Williams *et al.*, 1975; Laufer *et al.*, 1976; Szewczyk, 1978; Krothapalli *et al.*, 2000; Petitjean & McLaughlin, 2003; Petitjean *et al.*, 2005; Gee *et al.*, 2013) suggesting that crackle may be associated with the Mach wave radiation mechanism known to occur in supersonic free-shear-flow turbulence, though it has been observed that flows radiating Mach waves may not radiate noise perceived to crackle (Krothapalli *et al.*, 2000).

It appears that crackle is correlated to signals with intermittent periods of steepened shock-like waves followed by weaker, longer, rounded rarefaction regions, but to what extent this character originates at the turbulent source or arises from nonlinear propagation effects is unclear. Ffowcs Williams *et al.* (1975) suggested that crackle originates at or near the source. Within the range that the acoustic measurements were made, Ffowcs Williams *et al.* (1975) demonstrated that crackle was independent of jet scale and propagation distance, which suggests that cumulative nonlinear propagation effects did not distort the signal. Visualizations do suggest that the radiated waves are steepened near the shear layer of the jet (Krothapalli *et al.*, 2000; Freund *et al.*, 2000; Darke & Freund, 2001; Nichols *et al.*, 2013) but the connection between the steepened signal footprint near the source and the signal observed in the acoustic field has not been addressed in detail. There is evidence that $S_k(p')$ does evolve with propagation distance (Szewczyk, 1978; Petitjean & McLaughlin, 2003; Petitjean *et al.*, 2005) with noticeable nonlinearity during its course. The variation of sound spectra with propagation distance indicates energy being transferred from mid-frequencies to low- and high-frequencies (Petitjean & McLaughlin, 2003; Petitjean

et al., 2005; Fiévet *et al.*, 2014). The expectation is that wave merging due to nonlinearity will increase low-frequency energy content, though there is no direct observation of this, and wave-steepening will contribute energy to high-frequency modes.

Weak-shock theory, when applied to the propagation of broadband noise, predicts a final wavetrain of N-waves (Lighthill, 1956; Pestorius & Blackstock, 1974; Freund *et al.*, 2000) with symmetric amplitude distribution (i.e. $S_k(p') = 0$), not the asymmetric, peaked signals linked to the perception of crackle noise. This suggests that skewness arises from some other factor than one-dimensional weak-shock propagation. Crighton (1986) showed that linear dispersion and attenuation coupled with nonlinear mechanisms will increase S_k with distance, which might explain the skewness variations observed by Szewczyk (1978), Petitjean & McLaughlin (2003), and Petitjean *et al.* (2005).

2.2 Objectives and outline

The present simulations are designed to provide a detailed description of the turbulence mechanisms and any near-field nonlinearity that leads to acoustic fields of the kind associated with the perception of crackle. The simulations resolve all the energetic scales with no sub-grid scale models, which would potentially affect important features of the flow field, such as the sharp shock-like compressions in the near acoustic field. Though the shock thickness is set by the viscosity for the parameters considered, there is a small, but finite numerical dissipation in the simulations which is expected to weakly thicken shocks. While jet noise is the most important engineering situation, we chose to study a temporally developing planar shear layer because it provides a clearer perspective of the root mechanisms of this sound generation.

Though the equations are frame invariant, some care is required in switching intuitively from the supersonic advection generating Mach-like waves in a frame attached to a nozzle to the corresponding phenomenon in a time-developing flow, where transient approximately stationary (on average) turbulence features are adjacent to a supersonic stream. This configuration can be considered a model for the near-nozzle region of a high-Reynolds-number jet, where the turbulence is concentrated in a weakly curved (for a typical round jet) shear layer between the high-speed potential core flow and the surrounding co-flow. Because the simulations focus on this small region, it does allow us to explicitly resolve a broader range of turbulence scales than could be represented in a full jet simulation. In essence, it provides a Reynolds number realistic representation of a piece of a high-Reynolds-number jet, and it therefore allows us to probe the sound generation mechanisms of high-Reynolds-number turbulence. It can be anticipated the acoustic far-field will not include the geometric propagation effect associated with a round jet, though this will not be a large effect for studying the very near acoustic field. The flow configuration is not ideally suited for making point-to-point comparisons with lab measurements because acoustic data is typically acquired at $\gtrsim 10D_j$ from the shear layer, much farther away than our simulations, and there is no direct experimental counterpart to temporally developing shear layers. We do expect that lab measurements would ‘see’ a steepened, skewed footprint of a weakly nonlinear signal. The nearly linear signal would continue to propagate with its peculiar, asymmetric character and undergo slow, cumulative nonlinear changes associated with propagation of this type. Near-field acoustic measurements support this hypothesis (Petitjean & McLaughlin, 2003; Petitjean *et al.*, 2005; Baars & Tinney, 2014; Fiévet *et al.*, 2014). The details related to the simulation configurations and numerical methods are provided in section 3.

Very near-field sound of the temporally developing flow does indeed exhibit a sound field with the hallmarks of crackle: $S_k(p') > 0.4$ with steepened, compressions in the sound field. Analysis of our database will show the key features of the near-field acoustics that lead to these characteristics. Key results of our simulations including shear layer characteristics, turbulence statistics, and the evolution of the Mach-like wavefield leading to the sound correlated to crackle is given in section 4. A supplementary higher-Reynolds number simulation for $M = 2.5$ shows that crackle is insensitive to Reynolds number.

In section 5 a formulation of skewness budget is given. The budgets for a nominally non-crackling and crackling, $M = 0.9$ and 2.5 , respectively, are compared and we show that for the low-speed case, the entropic contribution to skewness is small (no shocks are present) and that skewness remains unchanged because acoustic mechanisms integrate roughly to zero. On the other hand, for $M = 2.5$, weak shocks are present in the acoustic field increasing the entropic sink of skewness. This sink is balanced by other acoustic mechanisms. The skewness here also remains unchanged suggesting the footprint of skewness,

a metric correlated to crackle, occurs at or very near the turbulent source.

3 Simulation details

3.1 Configuration

The three-dimensional compressible flow equations in Cartesian coordinates were solved for the temporally developing shear layer shown in figure 1. The details of the full governing equations are provided in appendix A. The flow domain dimensions are $L_x \times L_y \times L_z = 120 \delta_m^o \times 200 \delta_m^o \times 80 \delta_m^o$, where δ_m^o is the initial momentum thickness,

$$\delta_m(t) = \frac{1}{\rho_\infty \Delta U^2} \int_{-L_y/2}^{L_y/2} \bar{\rho}(\frac{1}{2} \Delta U - \tilde{u})(\frac{1}{2} \Delta U + \tilde{u}) dy, \quad (2)$$

at time $t = 0$. In (2), $\bar{(\)}$ and $\tilde{(\)}$ indicate Reynolds and Favre averages, respectively. The Reynolds number

$$Re_{\delta_m} = \frac{\rho_\infty \Delta U \delta_m(t)}{\mu}, \quad (3)$$

was $Re_{\delta_m} = 60$ initially and reached 2100 when $\delta_m(t)/\delta_m^o = 35$. A supplementary simulation at an initial Reynolds number of $Re_{\delta_m^o} = 120$ for $M = 2.5$ was simulated until $Re_{\delta_m} = 4000$. Details regarding this simulation are given in appendix C.

The planar shear layer was initialized with divergence-free velocity perturbations using the approach of Kleinman & Freund (2008) added to a streamwise velocity profile given by

$$\bar{u}(y) = \frac{\Delta U}{2} \tanh\left(5 \frac{y}{\delta_m^o}\right). \quad (4)$$

Four flow speeds— $M = 0.9, 1.5, 2.5$, and 3.5 —were simulated until the momentum thickness reached 35 times the initial momentum thickness. The Mach number is defined as $M = \Delta U/c_\infty$, where ΔU is the velocity difference between the free-streams. The $M = 0.9, 1.5$, and 3.5 cases were initialized by rescaling the $M = 2.5$ velocity field to their respective freestream velocity values.

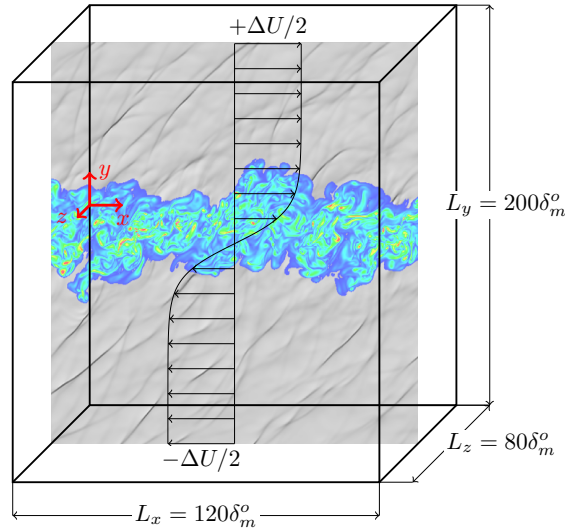


Figure 1: Simulation schematic.

3.2 Numerical methods

This domain was discretized with $N_x \times N_y \times N_z = 1536 \times 2048 \times 512$ mesh points. The solution was integrated in time using a standard fourth-order Runge–Kutta method. Derivatives in the periodic streamwise (x) and cross-stream (y) directions are computed with resolution-optimized finite differences. For the x -derivative, the fourth-order, dispersion-relation-preserving scheme of Tam & Webb (1993) was used. Though Fourier methods could have been used in the x -periodic direction, a local finite-difference method was chosen to be more computationally efficient than the global Fourier method since the domain was parallelized in this direction. The y -derivative was computed with an eighth-order pentadiagonal compact finite-difference scheme (Lele, 1992). Both x - and y -second derivatives were approximated using a maximum-order explicit sixth-order scheme. Near-boundary grid points in the y -direction had reduced-order central differences and one-sided differences at the domain extent. It is assumed that the low-order boundary closure methods for the derivatives are not expected to degrade the solution since they are far from the turbulence and inside absorbing sponge zones whose effect will be discussed later. The periodic spanwise z -direction used Fourier methods for both first and second derivatives. Details with regard to each numerical method are found in appendix B.

Fourier analysis of the finite-difference approximations provides an approximate dispersion relation to compare to the exact relation. Figure 2 and 3 shows the resolution properties of the first and second derivatives, respectively.

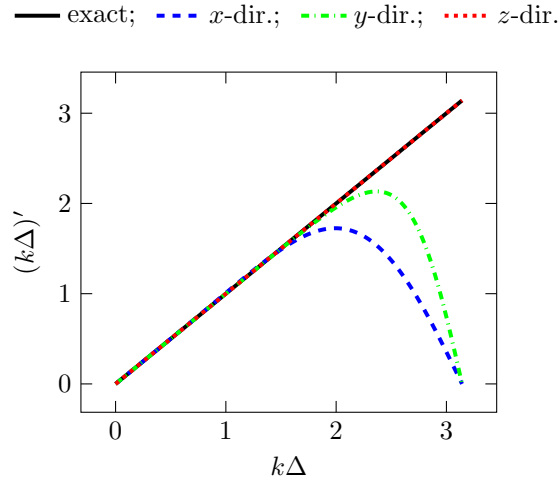


Figure 2: Modified wave number $(k\Delta)'$ resolution of first-order derivatives.

Because of finite computational resources, the domain in the y -direction must be truncated, and it is desired that the computational boundary mimics the properties of a radiation boundary conditions (i.e. no numerical reflections into the domain having a harmful effect on the solution). Experience has shown for flows of this kind (Kleinman & Freund, 2008) that a combination of an absorbing sponge region (Freund, 1997b) with one-dimensional characteristic radiation boundary conditions (Thompson, 1987) can achieve the radiation-like behavior provided the amplitude of fluctuating quantities leaving the domain is sufficiently small. Sponge regions of width $w_s = 44 \delta_m^o$ are modeled at $y = \pm L_y/2$ by adding a source term to the right-hand-side of the governing equations of the form

$$-\xi(y)(\mathbf{q} - \mathbf{q}_{\text{target}}). \quad (5)$$

The target solution vector is defined as

$$\mathbf{q}_{\text{target}} = \left[\rho_\infty, \rho_\infty \frac{\Delta U}{2}, 0, 0, \frac{p_\infty}{\gamma - 1} + \frac{1}{2} \rho_\infty \left(\frac{\Delta U}{2} \right)^2 \right], \quad (6)$$

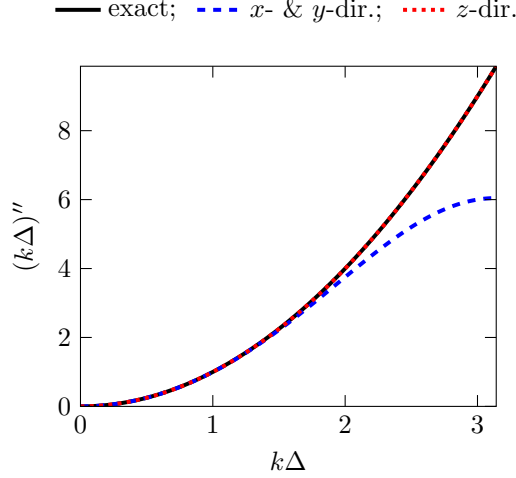


Figure 3: Modified wave number $(k\Delta)''$ resolution of second-order derivatives.

which forces the solution vector \mathbf{q} to the desired ambient boundary conditions. The sponge strength is quadratically increasing toward the domain extent given by

$$\xi(y) = \begin{cases} \frac{1}{2} \left[\frac{|y| - \left(\frac{L_y}{2} - w_s\right)}{w_s} \right]^2, & |y| > \frac{L_y}{2} - w_s \\ 0, & \text{otherwise} \end{cases} \quad (7)$$

To suppress the mild instabilities these numerical schemes are known to have, high-resolution numerical filtering was applied in all three coordinate directions, as is often done (Kleinman & Freund, 2008). In the spanwise direction, the top 20% of wave numbers of the Fourier transformed solution were filtered to zero. Explicit and implicit filtering as designed by Lele (1992) was used in the x - and y -directions, respectively. In x , the coefficients of the fourth-order scheme were chosen so the transfer function, equation (C.2.2) in Lele (1992), is $T(k) = 0.99$ at wavenumber $k = 1 \delta_m^o$. In y , the coefficients of the sixth-order scheme resulted $T(k) = 0.95$ at $k = 2 \delta_m^o$ and $T(k) = 0.5$ at $k = 2.6 \delta_m^o$. The filtering was done on the entire solution at each time step. Numerical tests which will explained later show that the filtering affects the high-wave-number range of the flow which contains little energy. The largest scales are unaffected by this stabilizing technique.

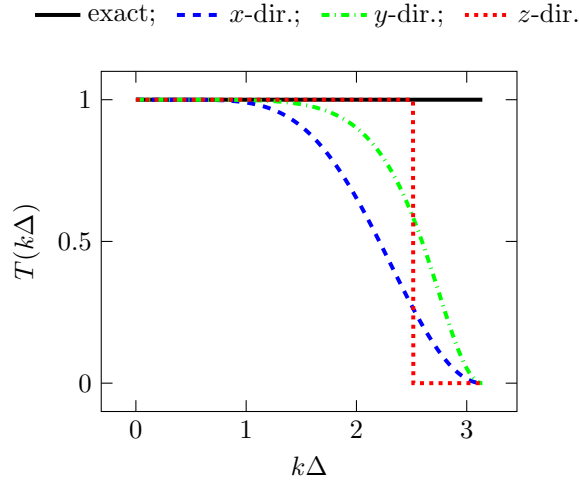


Figure 4: Transfer function $T(k\Delta)$ of selective high-wavenumber filtering schemes.

4 Results

4.1 Turbulence statistics

The growth of turbulent shear layers shown in figure 5. Though there is an initial transient, which is known to occur for simulations of this kind (Pantano & Sarkar, 2002; Kleinman & Freund, 2008), the growth appears approximately linear compared to the regression between $20 < \delta_m(t)/\delta_m^o < 35$.

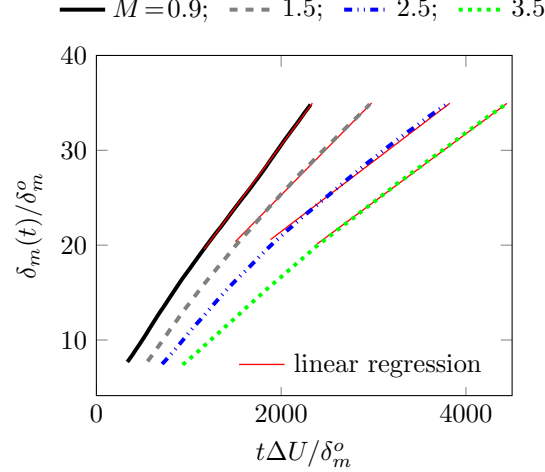


Figure 5: Shear layer growth with linear regression for $\delta_m(t)/\delta_m^o > 20$.

Taking the time derivative of equation 2 and neglecting molecular dissipation effects on the mean flow, the momentum thickness growth rate is

$$\dot{\delta}_m(t) = -\frac{2}{\rho_\infty \Delta U^2} \int_{-L_y/2}^{L_y/2} \widetilde{\rho u'' v''} \frac{\partial \tilde{u}}{\partial y} dy, \quad (8)$$

where $(\tilde{\cdot})$ represents the fluctuation by subtracting the Favre average from the total. Figure 6 shows the growth rate of the simulations compares well with spatially developing experiments (Elliott & Samimy, 1990; Goebel & Dutton, 1991; Debisschop *et al.*, 1994) and simulation (Pantano & Sarkar, 2002; Kleinman & Freund, 2008). As expected, shear layer growth is suppressed with increasing M and compares well with previous results.

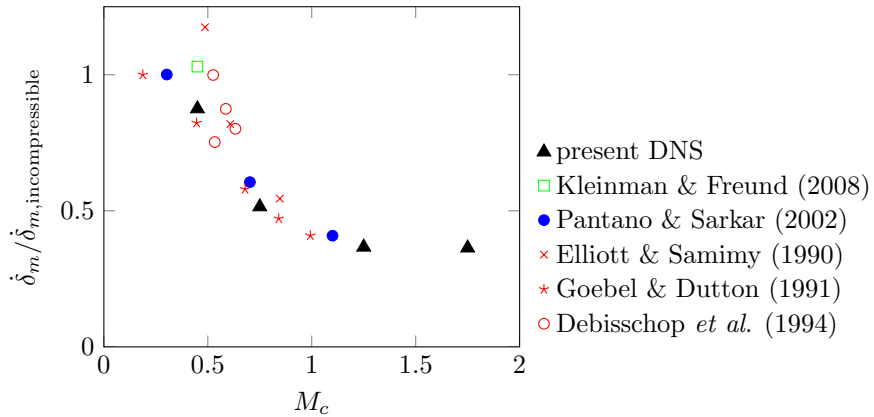


Figure 6: Shear layer growth rate.

Table 1 compares spatial resolution of previous compressible shear layers simulations. For the present simulations, the resolution coupled with a sufficiently low Reynolds number is expected to be adequately resolved.

Reference	M_c	$Re_{\delta_m^o}$	$\Delta x/\delta_m^o$	$\Delta y_{\min}/\delta_m^o$	$\Delta z/\delta_m^o$
Pantano & Sarkar (2002)	0.3-0.7	160	0.672	0.672	0.672
Pantano & Sarkar (2002)	1.1	160	0.675	0.675	0.677
Kleinman & Freund (2008)	0.9	69	2.94	2.34	4.49
Kleinman & Freund (2008)	0.9	207	0.976	0.79	1.47
Kleinman & Freund (2008)	0.9	414	0.976	0.79	1.47
Zhou <i>et al.</i> (2012)	0.7	100	0.673	0.775	0.631
present DNS	0.9-3.5	60	0.94	1.09	1.88
present DNS	2.5	120	0.5	0.5	0.5

Table 1: Comparison of resolution.

Figure 7 shows the spectrum of velocity fluctuations at $y = 0$, the midplane of the mixing layer. The turbulence is broadband and appears realistic.

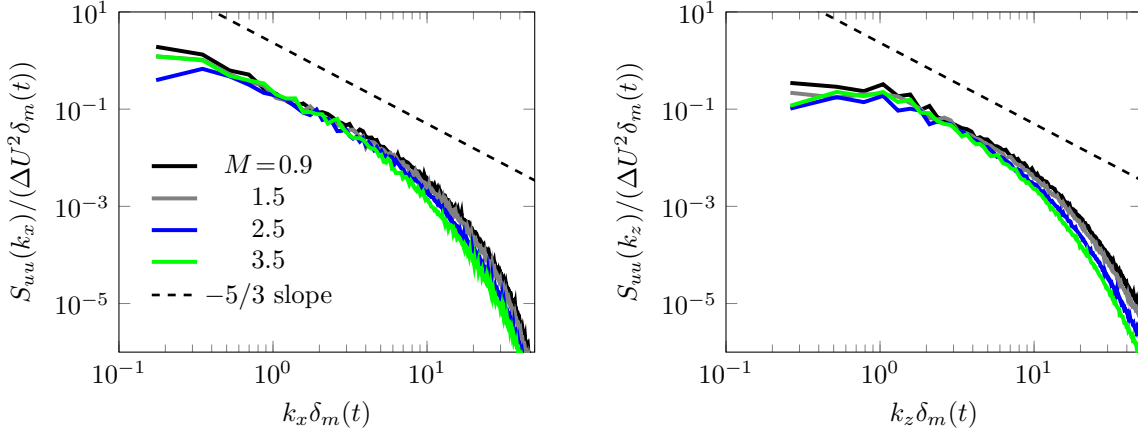


Figure 7: One-dimensional spectra of u -velocity fluctuations at $y = 0$ when $\delta_m(t)/\delta_m^o = 35$ in the (a) streamwise and (b) spanwise direction.

Figure 8 shows the effect the numerical stabilization method has on the highest wavenumbers. There is no apparent effect on the largest, energy-containing scales.

The peak turbulence intensities are compared with previous experiment (Elliott & Samimy, 1990; Goebel & Dutton, 1991; Debisschop *et al.*, 1994) and simulation (Pantano & Sarkar, 2002; Kleinman & Freund, 2008) in figure 9. As expected, the basic trend of the intensities decreases with increasing M_c . Average Reynolds stress profiles esemble averaged in time during approximate linear growth between $\delta_m(t)/\delta_m^o = 20$ and 35 are shown in figure 10.

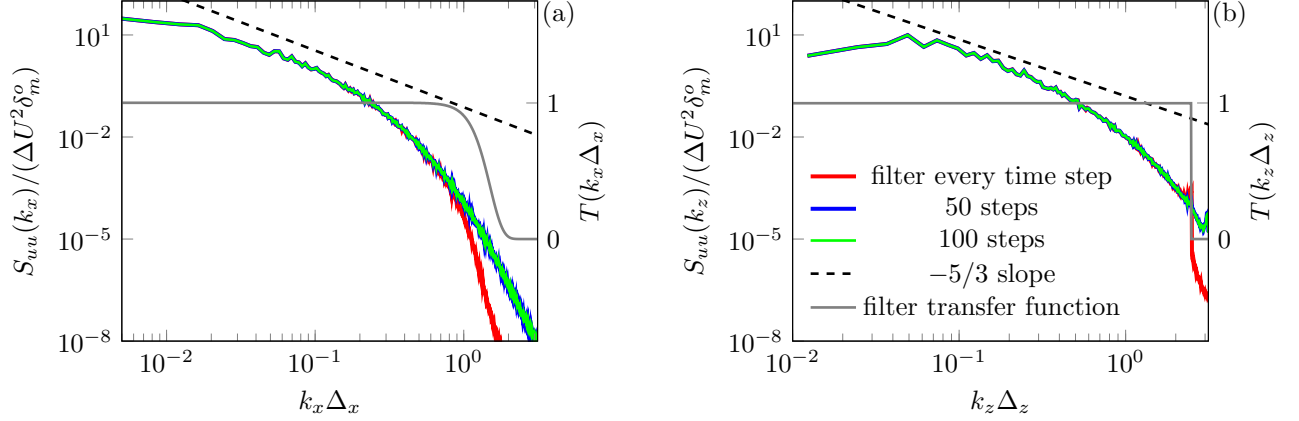


Figure 8: One-dimensional spectra of u -velocity fluctuations at $y = 0$ when $\delta_m(t)/\delta_m^o = 35$ for $M = 2.5$ in the (a) streamwise and (b) spanwise direction. The comparison between the number of time steps between filter applications is made after one flow-through time, $t_{fl} = 1440 \delta_m^o/\Delta U$.

The Reynolds stress profiles for $M = 0.9$ -3.5 are shown in figures 11-14. For higher Mach numbers $M \gtrsim 1.5$, the self-similar collapse of the profiles is not as obvious for the $M = 0.9$.

4.2 Near-field acoustics

Whether or not $S_k(p')$ is a useful metric for the perception of crackle, it is undoubtedly a peculiar feature of the sound field. We start by confirming that the simulations do produce this hallmark feature of nominally crackling jets. Figure 15 shows that $S_k(p')$ at all y increases with M . This appears to happen continuously, without a distinct transition to finite S_k and nominally ‘crackling’ behavior, though the discrete M simulated does not preclude this. For $M \geq 2.5$, the $S_k(p')$ exceeds 0.4 expected for turbulent jets. All statistics presented throughout this section have been averaged over the x - and z -directions and ensemble averaged in time between $t\Delta U/\delta_m(t) = 1500$ and 2500.

For any M , into the very near acoustic field, we observe an approximately constant $S_k(p')$. This may seem to contradict the evidence that skewness increases with propagation distance (Szewczyk, 1978; Petitjean & McLaughlin, 2003; Petitjean *et al.*, 2005), though significant variation is not expected for the propagation distances we consider here.

Figure 16 shows typical pressure traces at different Mach numbers. These have sharper compressive peaks than expansions for the highest speeds, especially the $M = 3.5$ case, which is comparable to experimental observation (Ffowcs Williams *et al.*, 1975; Laufer *et al.*, 1976; Szewczyk, 1978; Krothapalli *et al.*, 2000; Baars & Tinney, 2014). Note that these pressure traces are close to the turbulence, at $y = 5.5 \delta_m$. Thus, skewed pressure signals and apparently steepened wave profiles exist very near the turbulence.

■ present DNS; ● Foysi & Sarkar (2010); ▲ Pantano & Sarkar (2002); + Bell & Mehta (1990);
 * Debisschop Bonnet (1993); * Elliott & Samimy (1990); * Goebel & Dutton (1991); * Wyganski & Fiedler (1970)

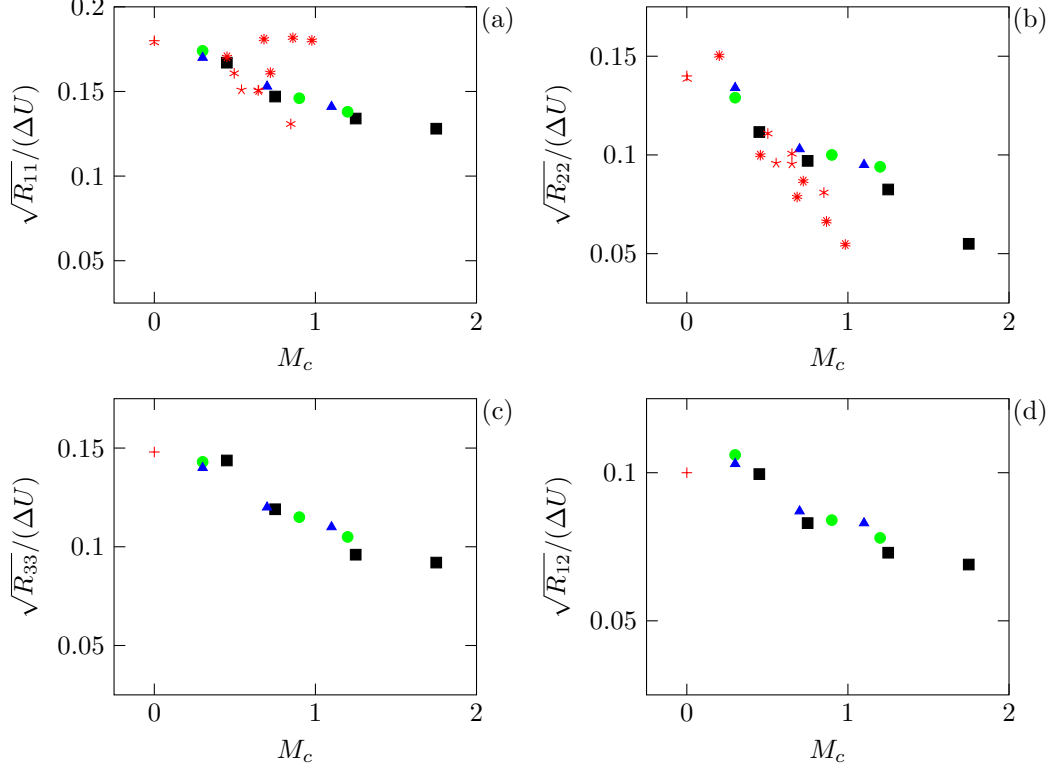


Figure 9: Peak turbulent intensities.

4.3 Near-field nonlinearity

Directional waves radiating from high-speed free-shear flows have been observed by schlieren and shadowgraph techniques for many years. The orientation of these directional waves provide a clue to the relative speed of the turbulence source that generates this Mach-like wave. Laufer (1961) used hot-wire anemometer techniques to measure u' -velocity perturbations in the acoustic field. His measurements also indicated that the fluctuations away from the turbulent boundary layer were solely acoustic ones. Duan *et al.* (2014) also provided correlations in the near acoustic field that suggest the Mach-like waves are backward-facing waves with $\langle u'p' \rangle \approx -1$ and that they are mainly acoustic, with negligible entropic and vortical contributions. Assuming a purely acoustic field with planar waves, Laufer (1961) used the linear relation between pressure and the particle velocity u'_n given here by

$$\frac{u'_n}{\bar{u}} = \frac{1}{M} \frac{p'}{\gamma \bar{p}} \quad (9)$$

and with the geometric relation between the horizontal and normal velocity perturbation

$$u' = u'_n \cos(\theta), \quad (10)$$

the orientation of wave can be calculated. The inferred angle from the measurements of u' agreed visually with the observed wave orientation in the near acoustic field (Laufer, 1961). Simulation of radiated sound from high-speed turbulent boundary layers shows a similar qualitative agreement using the same analysis (Duan *et al.*, 2014).

Using a time-delay cross-correlation of the pressure field between two measurement points, Nichols *et al.* (2013) indirectly measured the angle of propagation, and the orientation qualitatively agrees with the orientation of the wave-like structures in the sound field.

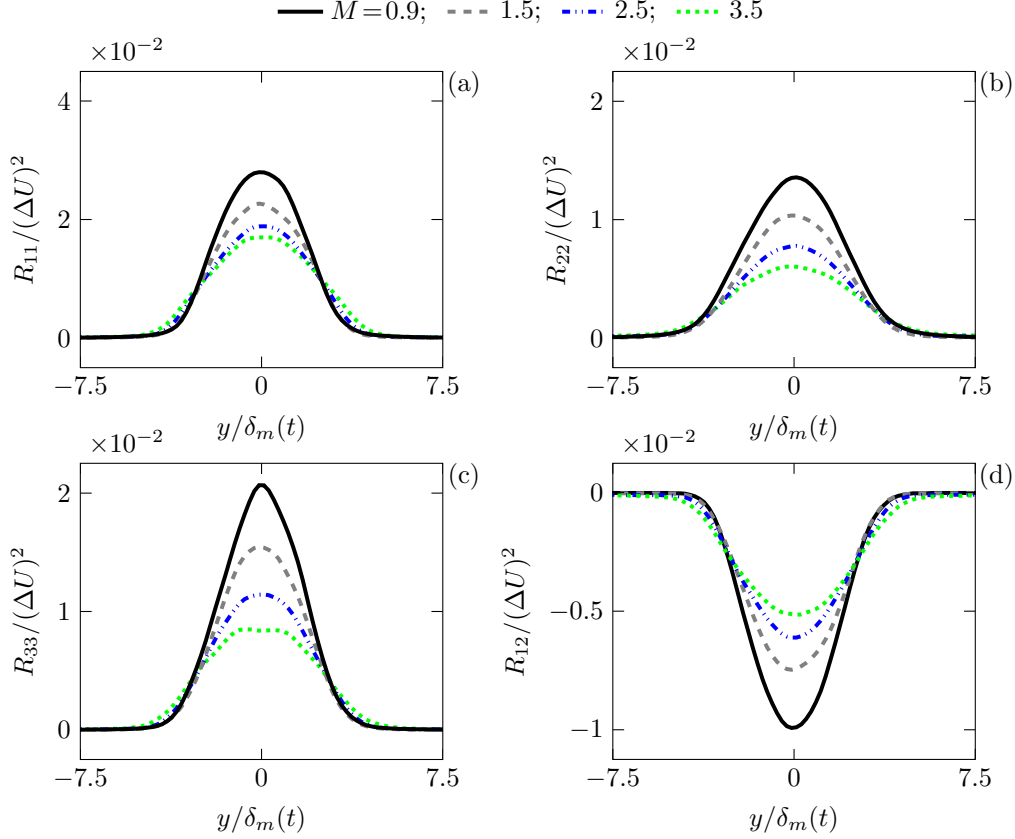


Figure 10: Average Reynolds stress profiles.

Our approach measures the angle of structures directly from the flow solution. Figure 17 shows the method for computing wave angle at a single point in the near acoustic field. The angle is given by

$$\theta = \cos^{-1} n_y, \quad (11)$$

where n_y is the y -component of the normal vector computed from the gradient of the pressure field

$$\mathbf{n} = \frac{\nabla p}{|\nabla p|}. \quad (12)$$

Wave angle statistics are chosen to be conditional on the strength of the compression specifically a dilatation threshold. Figures 18-20 show the average wave angle conditioned on dilatation threshold for $M = 1.5, 2.5$ and 3.5 . The $M = 0.9$ case was omitted from these results because Mach wave radiation is not expected to occur and the sound field for $M = 0.9$ did not have sufficient compressions for the range of dilatation thresholds considered to accrue converged statistics. Based on the proposed mechanism of Mach wave radiation from high-speed turbulent shear layers (Phillips, 1960; Ffowcs Williams & Maidanik, 1965), it is expected that the mean wave angle in the near acoustic field decreases with increasing flow speed: $\langle \theta \rangle = 55^\circ, 34^\circ$, and 27° at $y = 15 \delta_m(t)$ for $M = 1.5, 2.5$, and 3.5 , respectively.

The range of wave angles are quantified by the standard deviations in figures 18-20. The width of one standard deviation suggests a range of source speeds within the turbulence. Smaller standard deviations about the mean are observed for slower speeds. For $M = 3.5$, in particular, the range of angles decreases with distance from the mixing layer. This would be consistent with the geometric flattening and possible merging of different waves due to weak-shock propagation nonlinearity.

Figure 21 shows the effect of varying the dilatation threshold on the average wave angle. For $M \gtrsim 2.5$, decreasing d_c which includes stronger waves suggests the trend of decreasing wave angle with distance

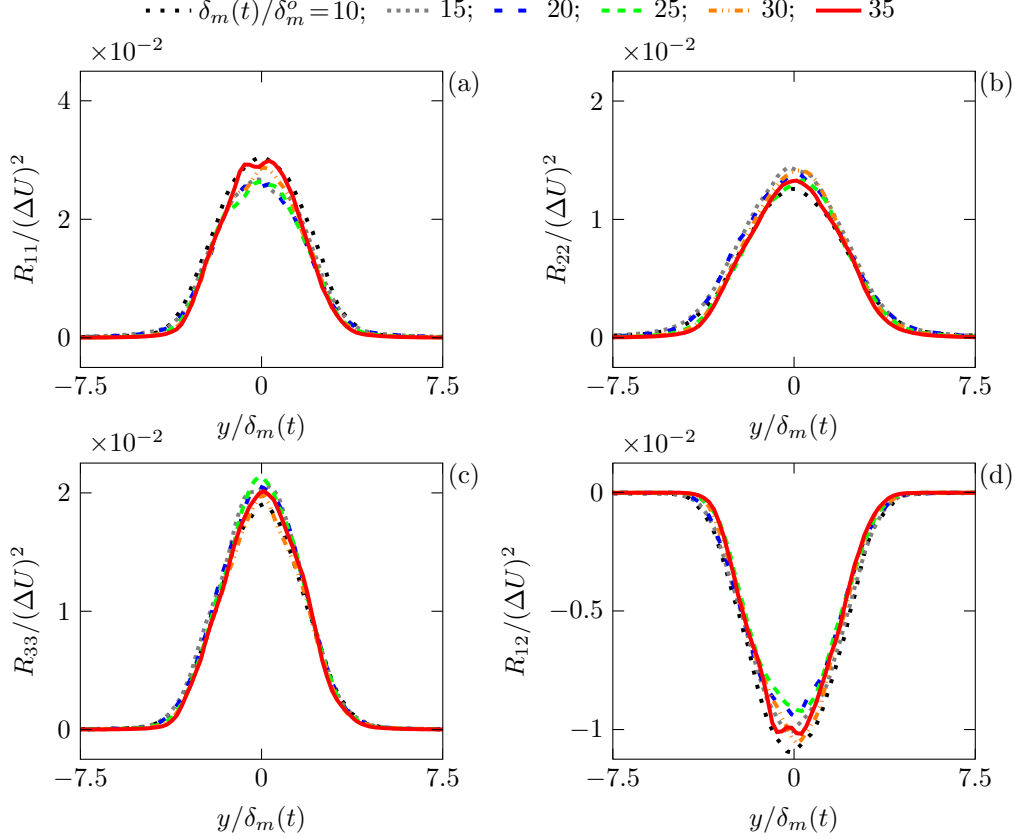


Figure 11: Reynolds stress profiles for $M = 0.9$ at different shear layer thicknesses.

is converging. For $M = 1.5$, the trend with distance seems to diverge primarily because less waves are being counted which is later confirmed in figure 23.

Cumulative propagation effects are anticipated to reduce the number of distinct waves (Lighthill, 1956). Described as ‘wave-bunching’, stronger shocks with a higher propagation velocity will ‘consume’ weaker, more slowly propagating ones (Lighthill, 1956, 1993). To quantify this wave-merging effect, we sum the number (N) of contiguous compression regions in the x -direction that satisfies the threshold condition, $\nabla \cdot \mathbf{u} \leq d_c$. We see in figure 22 a qualitatively different evolution of wave density between the $M = 1.5$ and the nominally crackling cases. The wave density in y increases for $M = 1.5$ because at earlier times the smaller scales of the turbulence produce more distinct waves. At larger y these shorter waves (and higher frequencies) persist. Nonlinear merging counters this. For $M = 2.5$ and 3.5 , the number of waves decreases into the acoustic field. The effect of varying d_c between -0.1 and $-0.003\delta_m(t)/\Delta U$ causes the $N\delta_m/L_x$ curves to shift downward as fewer waves are being counted, though the shape remains unchanged.

The effect of dilatation threshold is again considered for the wave counting as shown in figure 23. Overall, the basic trends with distance from the centerline is captured regardless of the dilatation threshold. The number of waves counted shifts vertically with decreasing d_c because fewer waves are being averaged. For the smallest dilatation threshold in $M = 0.9$, the trend with distance is not preserved because the number of waves contributing to the mean is so small.

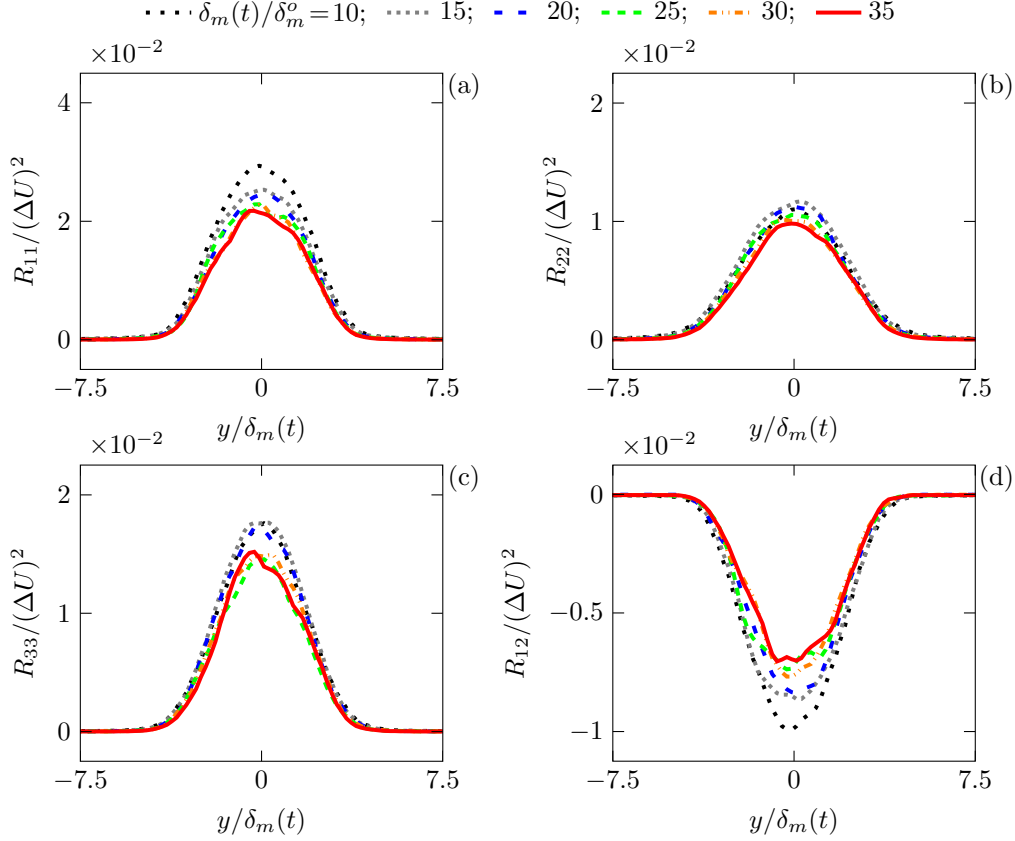


Figure 12: Reynolds stress profiles for $M = 1.5$ at different shear layer thicknesses.

The statistics of mean wave angle and scaled wave density suggest waveforms undergo nonlinear interactions in the near acoustic field. Visualization and tracking of individual wave fronts confirm that waveforms nonlinearly interact and merge into a single wave front in figure 24.

The two-point correlation of fluctuating pressure,

$$C_{p'p'}(\boldsymbol{\delta}, t) = \langle p'(\mathbf{x} + \boldsymbol{\delta}, t)p'(\mathbf{x}, t) \rangle, \quad (13)$$

provides a measure of the mean wave structure. We consider a two-dimensional correlation in which $\boldsymbol{\delta} = (\delta_x, \delta_y, 0)$. The integral length scale,

$$\mathcal{L}_w(\xi, t) = \frac{1}{\langle (p')^2 \rangle} \int C_{p'p'}(\delta_x, \delta_x \tan(\xi), 0, t) d\delta_x, \quad (14)$$

along a line inclined at angle ξ is shown in figure 26. For $M = 3.5$ case the length of the wave grows with increasing distance from the turbulence (figure 26) as would be consistent for merging waves.

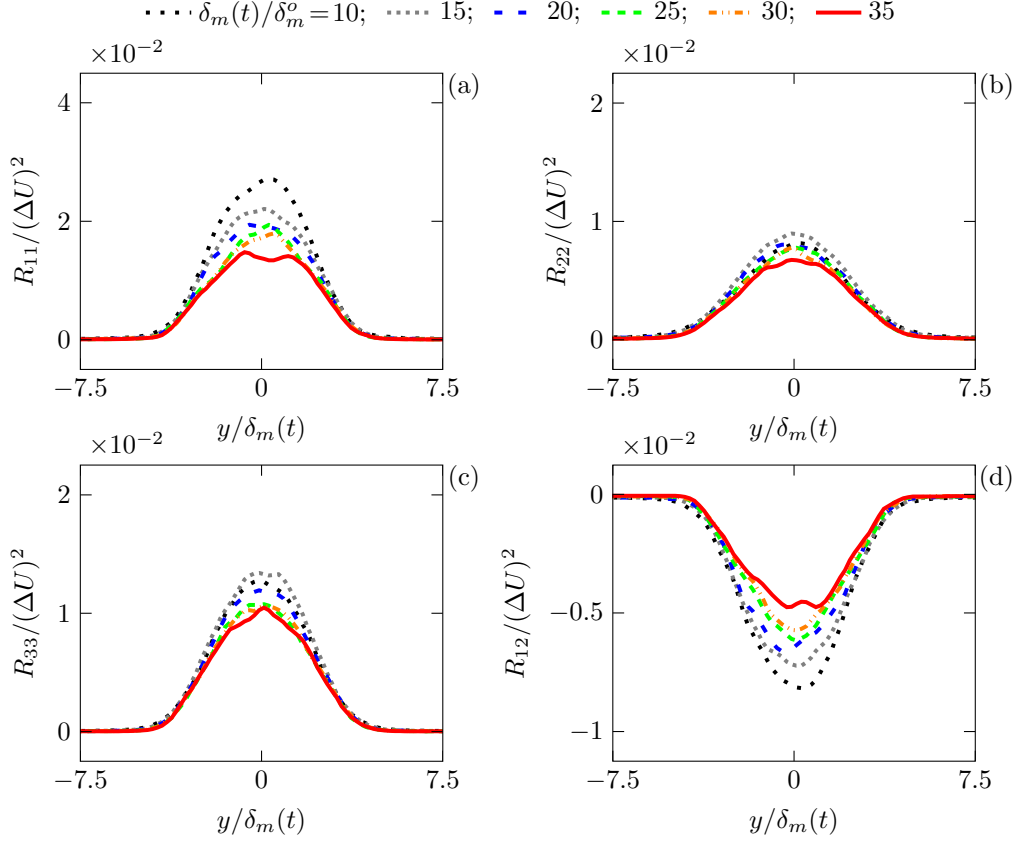


Figure 13: Reynolds stress profiles for $M = 2.5$ at different shear layer thicknesses.

5 Pressure variance and skewness budget

5.1 Derivation

Thermodynamic quantities are generally expressed as a function of any two thermodynamic quantities. The pressure is written as a function of density and entropy

$$p = p(\rho, S), \quad (15)$$

and it follows that

$$\frac{Dp}{Dt} = \left(\frac{\partial p}{\partial \rho} \right)_S \frac{D\rho}{Dt} + \left(\frac{\partial p}{\partial s} \right)_\rho \frac{DS}{Dt}, \quad (16)$$

where the operator D/Dt is defined as

$$\frac{D}{Dt} \equiv \frac{\partial}{\partial t} + u_i \frac{\partial}{\partial x_i} \quad (17)$$

Assuming an ideal gas, the thermodynamic relations are given as

$$\begin{aligned} \left(\frac{\partial p}{\partial \rho} \right)_S &= -c^2 \rho \\ \left(\frac{\partial p}{\partial s} \right)_\rho &= -\frac{p}{c_v}, \end{aligned} \quad (18)$$

where c_v is the specific heat at constant volume and c is the isentropic speed of sound given as

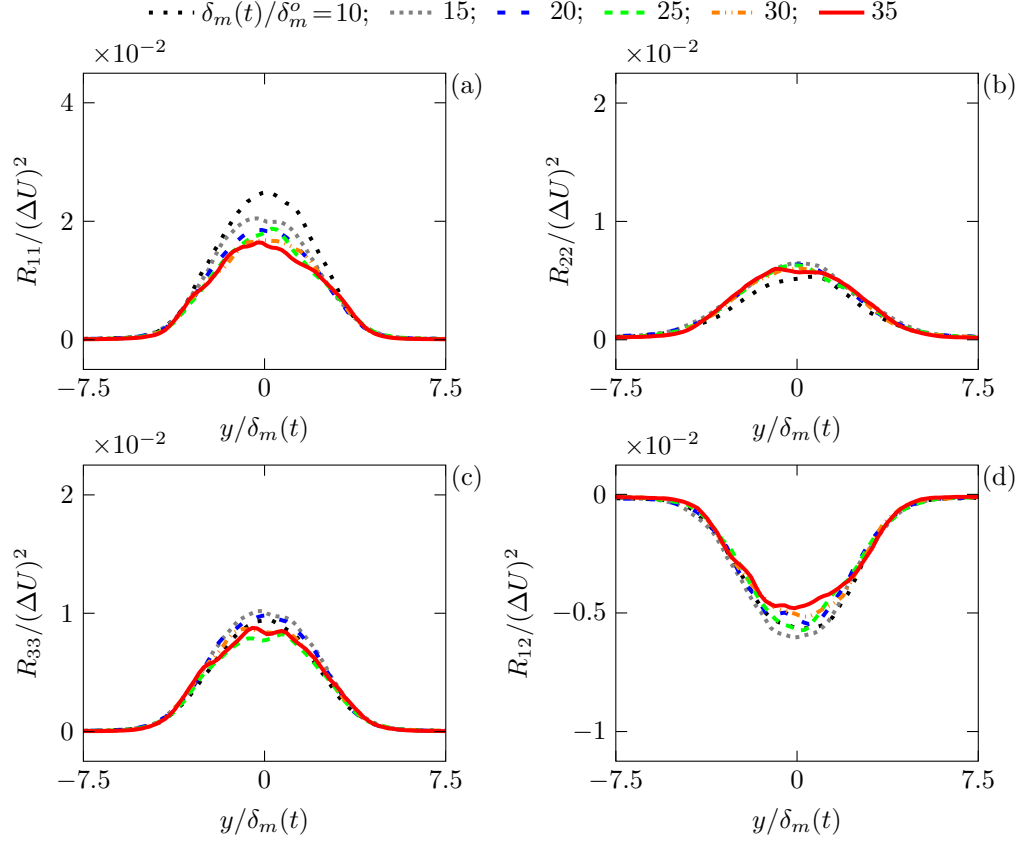


Figure 14: Reynolds stress profiles for $M = 3.5$ at different shear layer thicknesses.

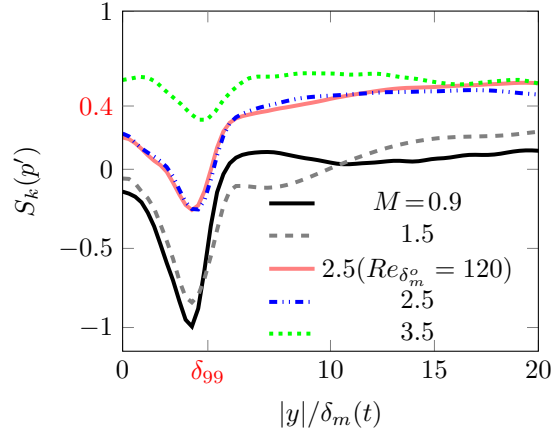


Figure 15: Variation of skewness with vertical distance from shear layer.

$$c^2 = \frac{\gamma p}{\rho} \quad (19)$$

Using conservation of mass to replace the material derivative of density, the equation for pressure is

$$\frac{Dp}{Dt} = \underbrace{-\gamma p \frac{\partial u_i}{\partial x_i}}_{\text{acoustic}} + \underbrace{-\frac{p}{c_v} \frac{DS}{Dt}}_{\text{entropic}}. \quad (20)$$

For now we will focus on the acoustic contributions to the pressure changes. To assess the magnitude

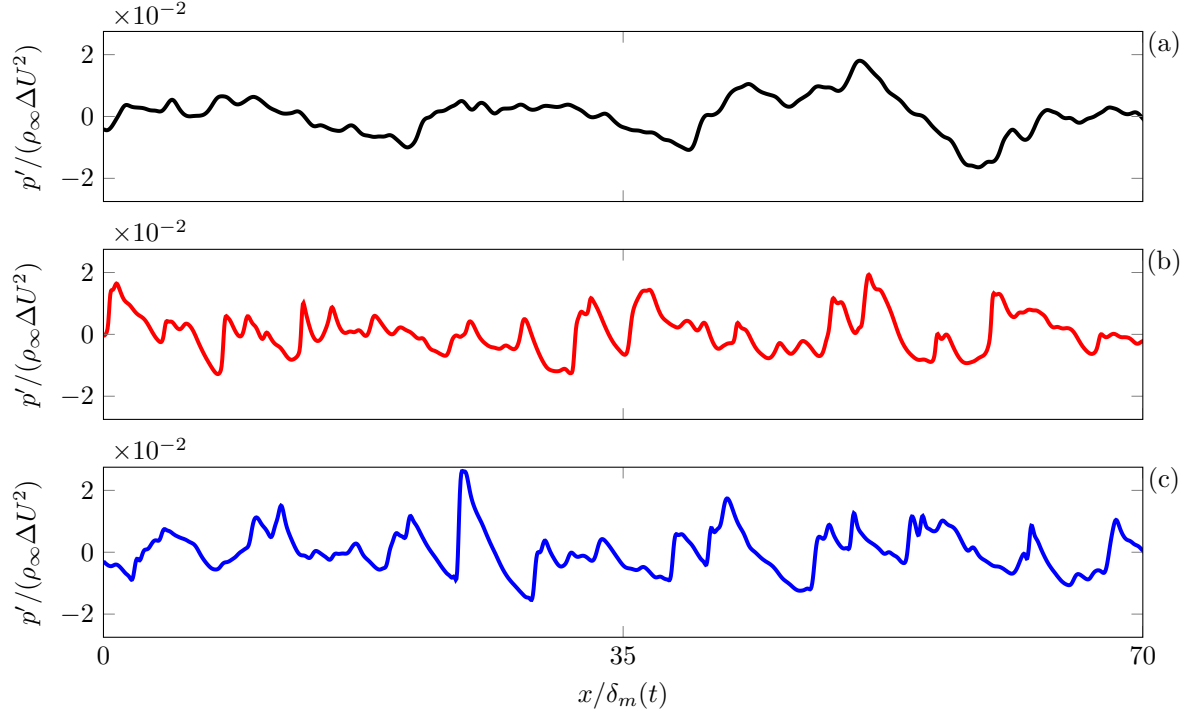


Figure 16: Fluctuation pressure trace at $\delta_m(t)/\delta_m^o = 5.5$ for (a) $M = 1.5$, (b) 2.5, and (c) 3.5.

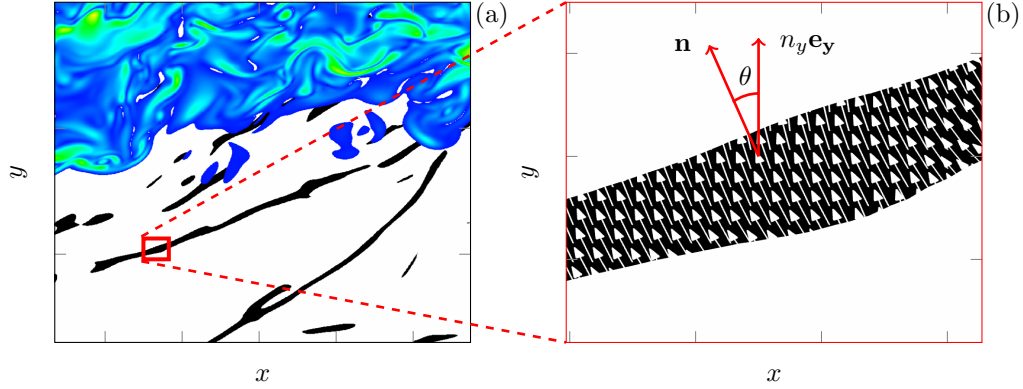


Figure 17: (a) Schematic of the very near field acoustic field with $\nabla \cdot \mathbf{u} < -0.0125$ below the vorticity magnitude colored between $|\nabla \times \mathbf{u}| = 0.1$ and $5\Delta U/\delta_m(t)$. (b) Detailed view of wavefront with normal vectors shown at each computational grid point.

of the entropic contributions, the left-hand-side of equation 20 will be directly computed from our DNS database. To find an evolution equation for pressure variance $((p')^2)$ and skewness $((p')^3)$, the variables must be Reynolds decomposed by

$$\begin{aligned} p &= p' + \bar{p} \\ u_i &= u'_i + \bar{u}_i, \end{aligned} \quad (21)$$

where $()'$ and $\bar{()}$ denote a fluctuation and an average. The method of averaging depends on the problem. For a parallel shear flow, the average is taken to be an ensemble average over the x - z plane at a given y . Substituting the Reynolds decomposition, the pressure equation is

$$\frac{D\bar{p} + p'}{Dt} = -\gamma(\bar{p} + p') \frac{\partial \bar{u}_i + u'_i}{\partial x_i} + \dots, \quad (22)$$

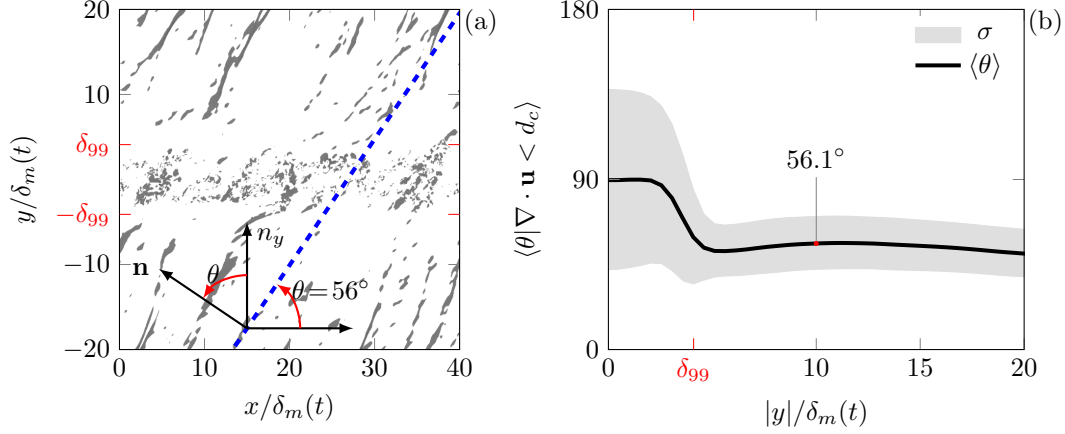


Figure 18: $M = 1.5$: (a) Dilatation, $(\nabla \cdot \mathbf{u})\delta_m(t)/\Delta U < -0.0125$, when $\delta_m(t)/\delta_m^o = 32.8$ at $z = L_z/2$. (b) Average wave angles ($\langle\theta\rangle$) conditioned on $(\nabla \cdot \mathbf{u})\delta_m(t)/\Delta U < -0.0125$ shaded by one standard deviation (σ) about the mean.

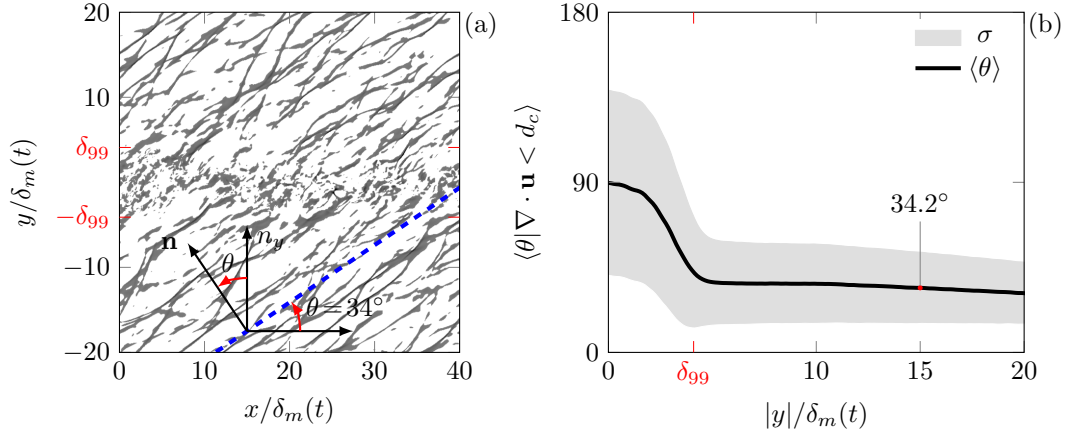


Figure 19: $M = 2.5$: (a) Dilatation, $(\nabla \cdot \mathbf{u})\delta_m(t)/\Delta U < -0.0125$, when $\delta_m(t)/\delta_m^o = 32.8$ at $z = L_z/2$. (b) Average wave angles ($\langle\theta\rangle$) conditioned on $(\nabla \cdot \mathbf{u})\delta_m(t)/\Delta U < -0.0125$ shaded by one standard deviation (σ) about the mean.

where (...) represent the entropic contribution which will not be explicitly written out here but will computed indirectly by evaluating the left-hand-side from the DNS database. For the rest of the exposition, the entropic components will be left out of the equations. Taking the average equation 22, the average pressure evolution is

$$\frac{\partial \bar{p}}{\partial t} + \bar{u}_i \frac{\partial \bar{p}}{\partial x_i} + \overline{u'_i \frac{\partial p'}{\partial x_i}} = -\gamma \left[\bar{p} \frac{\partial \bar{u}_i}{\partial x_i} + \overline{p' \frac{\partial u'_i}{\partial x_i}} \right]. \quad (23)$$

Again using Reynolds decomposition, the evolution of fluctuating pressure is given as

$$\frac{\partial p'}{\partial t} = \frac{\partial p}{\partial t} - \frac{\partial \bar{p}}{\partial t}, \quad (24)$$

and by substituting the full and mean pressure equation, the fluctuating pressure is

$$\frac{\partial p'}{\partial t} = -\bar{u}_i \frac{\partial p'}{\partial x_i} - u'_i \frac{\partial \bar{p}}{\partial x_i} - u'_i \frac{\partial p'}{\partial x_i} + \overline{u'_i \frac{\partial p'}{\partial x_i}} - \gamma \left[\bar{p} \frac{\partial u'_i}{\partial x_i} + p' \frac{\partial \bar{u}_i}{\partial x_i} + p' \frac{\partial u'_i}{\partial x_i} \right] + \gamma \overline{p' \frac{\partial u_i}{\partial x_i}} \quad (25)$$

With the evolution equation for fluctuation pressure, the high-order moment equations for the variance skewness can be written as

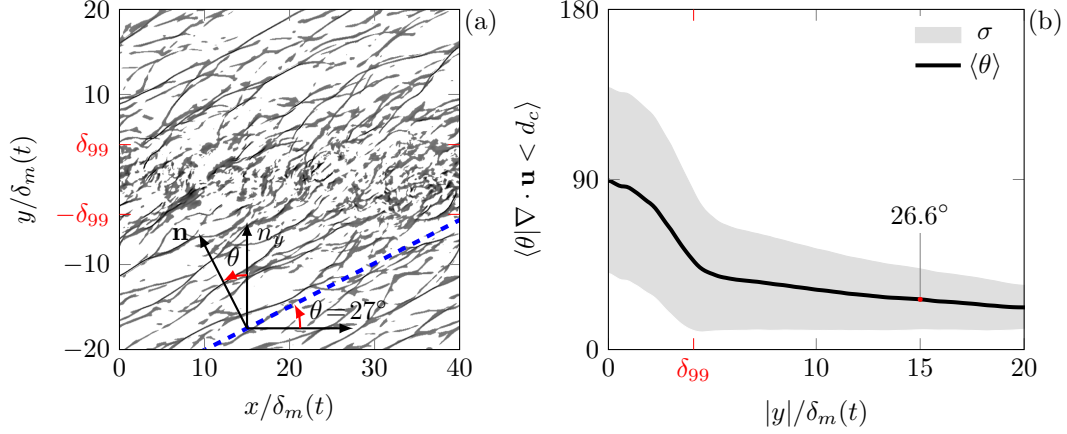


Figure 20: $M = 3.5$: (a) Dilatation, $(\nabla \cdot \mathbf{u})\delta_m(t)/\Delta U < -0.0125$, when $\delta_m(t)/\delta_m^o = 32.8$ at $z = L_z/2$. (b) Average wave angles ($\langle\theta\rangle$) conditioned on $(\nabla \cdot \mathbf{u})\delta_m(t)/\Delta U < -0.0125$ shaded by one standard deviation (σ) about the mean.

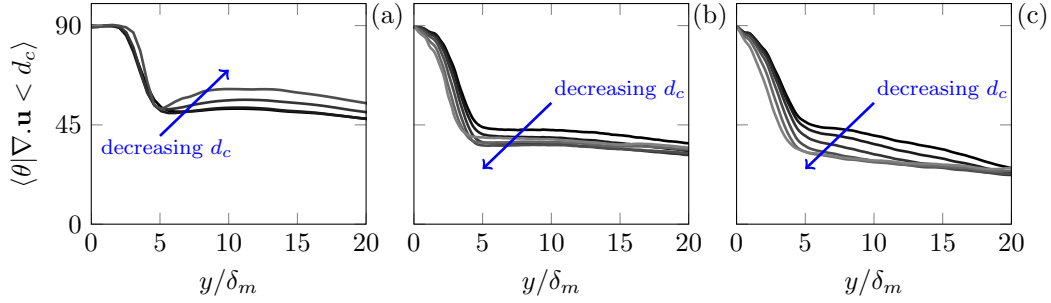


Figure 21: Variation of average wave angle with dilatation threshold for (a) $M = 1.5$, (b) 2.5, and (c) 3.5. The various values of d_c shown range between -0.0125 and -0.003125.

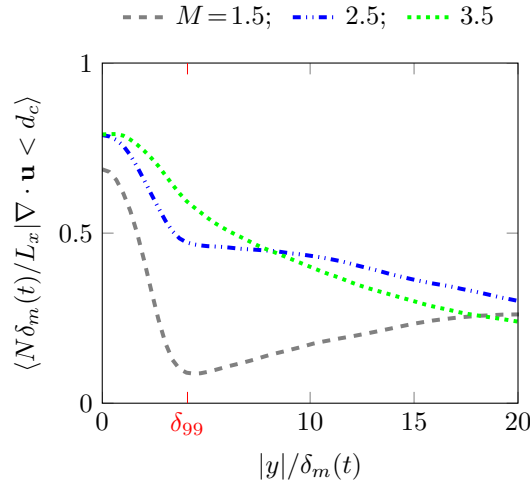


Figure 22: Scaled average number of waves conditioned on $(\nabla \cdot \mathbf{u})\delta_m(t)/\Delta U < -0.0125$.

$$\begin{aligned} \overline{\frac{\partial(p')^2}{\partial t}} &= 2\overline{p' \frac{\partial p'}{\partial t}} \\ \overline{\frac{\partial(p')^3}{\partial t}} &= 3\overline{(p')^2 \frac{\partial p'}{\partial t}} \end{aligned} \quad (26)$$

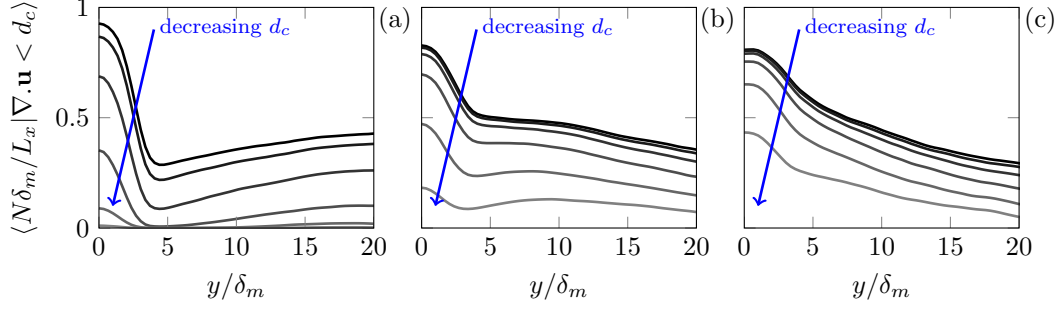


Figure 23: Variation of scaled average number of waves with dilatation threshold for (a) $M = 1.5$, (b) 2.5, and (c) 3.5. The various values of d_c shown range between -0.0125 and -0.003125.

respectively. Multiplying the equation 25 by $2p'$ and taking the average, the pressure variance equation is

$$\begin{aligned} \frac{\partial \overline{(p')^2}}{\partial t} = & -2\overline{u_i p'} \frac{\partial p'}{\partial x_i} - 2\frac{\partial \overline{p}}{\partial x_i} \overline{u'_i p'} - 2\overline{u'_i p'} \frac{\partial p'}{\partial x_i} \\ & - 2\gamma \left[\overline{p} \frac{\partial u_i}{\partial x_i} p' + \frac{\partial \overline{u_i}}{\partial x_i} \overline{(p')^2} + \overline{(p')^2} \frac{\partial u'_i}{\partial x_i} \right]. \end{aligned} \quad (27)$$

Moving the first term on the right hand side to the left we can define

$$\frac{\overline{D}}{Dt} \overline{(p')^2} \equiv \frac{\partial \overline{(p')^2}}{\partial t} + \overline{u_i} \frac{\partial \overline{(p')^2}}{\partial x_i}, \quad (28)$$

leaving

$$\frac{\overline{D}}{Dt} \overline{(p')^2} = -2\frac{\partial \overline{p}}{\partial x_i} \overline{u'_i p'} - 2\overline{u'_i p'} \frac{\partial p'}{\partial x_i} - 2\gamma \left[\overline{p} \frac{\partial u_i}{\partial x_i} p' + \frac{\partial \overline{u_i}}{\partial x_i} \overline{(p')^2} + \overline{(p')^2} \frac{\partial u'_i}{\partial x_i} \right].$$

The equation for pressure variance differs from Sarkar (1992) (see equation 7) and could be made identical by invoking the following relation

$$\frac{\partial p' p' u'_i}{\partial x_i} = 2p' u'_i \frac{\partial p'}{\partial x_i} + (p')^2 \frac{\partial u'_i}{\partial x_i}. \quad (29)$$

Performing the same manipulations for pressure skewness we have

$$\begin{aligned} \frac{1}{3} \frac{\partial \overline{(p')^3}}{\partial t} + \frac{1}{3} \overline{u_i} \frac{\partial \overline{(p')^3}}{\partial x_i} = & -\frac{\partial \overline{p}}{\partial x_i} \overline{u'_i (p')^2} - \overline{u'_i (p')^2} \frac{\partial p'}{\partial x_i} + \overline{(p')^2} u'_i \frac{\partial p'}{\partial x_i} \\ & + \gamma \left[-\overline{p} \frac{\partial u_i}{\partial x_i} (p')^2 - \frac{\partial \overline{u_i}}{\partial x_i} \overline{(p')^3} - \overline{(p')^3} \frac{\partial u'_i}{\partial x_i} + p' \frac{\partial u'_i}{\partial x_i} \overline{(p')^2} \right]. \end{aligned} \quad (30)$$

Using a simplifying relation

$$\frac{\partial p' p' p' u'_i}{\partial x_i} = 3(p')^2 u'_i \frac{\partial p'}{\partial x_i} + (p')^3 \frac{\partial u'_i}{\partial x_i}, \quad (31)$$

the equation for skewness is

$$\begin{aligned} \frac{\overline{D}}{Dt} \overline{(p')^3} = & -3\frac{\partial \overline{p}}{\partial x_i} \overline{u'_i (p')^2} - \frac{\partial \overline{(p')^3} u'_i}{\partial x_i} + (p')^3 \frac{\partial u'_i}{\partial x_i} + 3\overline{(p')^2} u'_i \frac{\partial p'}{\partial x_i} \\ & + 3\gamma \left[-\overline{p} \frac{\partial u_i}{\partial x_i} (p')^2 - \frac{\partial \overline{u_i}}{\partial x_i} \overline{(p')^3} - \overline{(p')^3} \frac{\partial u'_i}{\partial x_i} + p' \frac{\partial u'_i}{\partial x_i} \overline{(p')^2} \right]. \end{aligned} \quad (32)$$

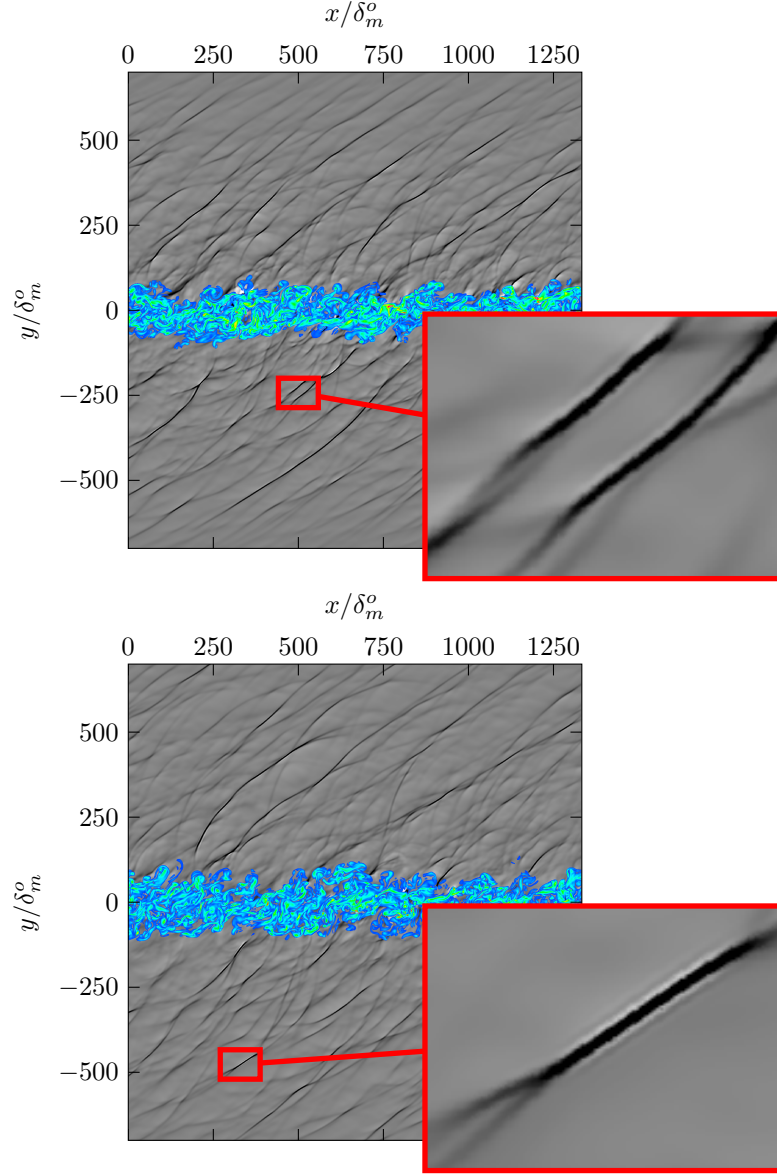


Figure 24: Visualizations of merging wave fronts for $M = 2.5$ when $\delta_m(t)/\delta_m^o = 15$ to 25 at $z = L_z/2$: color contours show $|\nabla \times \mathbf{u}|$ between 0.1 and $5\Delta U/\delta_m(t)$ and gray-scale contours show $\nabla \cdot \mathbf{u}$ between $\pm 0.5\Delta U/\delta_m(t)$.

The entire equation can be normalized by $\overline{(p')^2}^{3/2}$ to give the evolution of normalized pressure skewness, $S_k(p')$. The skewness and variance evolution equations are general for any flow configuration. We will specialize them to a parallel shear flow where only derivatives of mean quantities in the y -direction are nonzero.

$$\begin{aligned} \frac{\overline{D}}{Dt} \overline{(p')^3} = & -3 \frac{\partial \overline{p}}{\partial y} \overline{v'(p')^2} - \frac{\partial \overline{(p')^3 v'}}{\partial y} + \overline{(p')^3 d'} + 3 \overline{(p')^2 u'_i} \frac{\partial p'}{\partial x_i} \\ & + 3\gamma \left[-\overline{p d'} \overline{(p')^2} - \frac{\partial \overline{v}}{\partial y} \overline{(p')^3} - \overline{(p')^3 d'} + \overline{p' d'} \overline{(p')^2} \right], \end{aligned} \quad (33)$$

where $d' = \partial u'_i / \partial x_i$ represents the fluctuating dilatation.

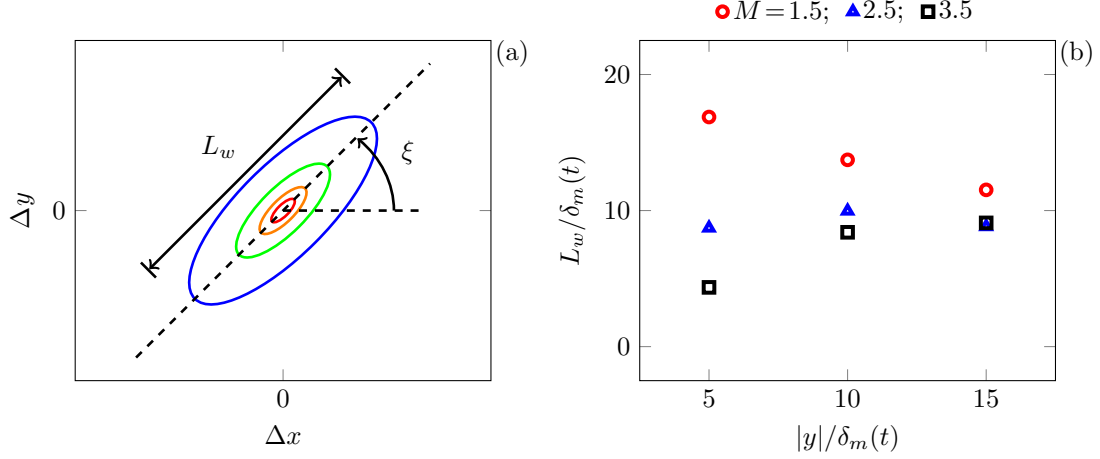


Figure 25: (a) Schematic of space-space correlation. (b) Integral length when $\delta_m(t)/\delta_m^o = 35$.

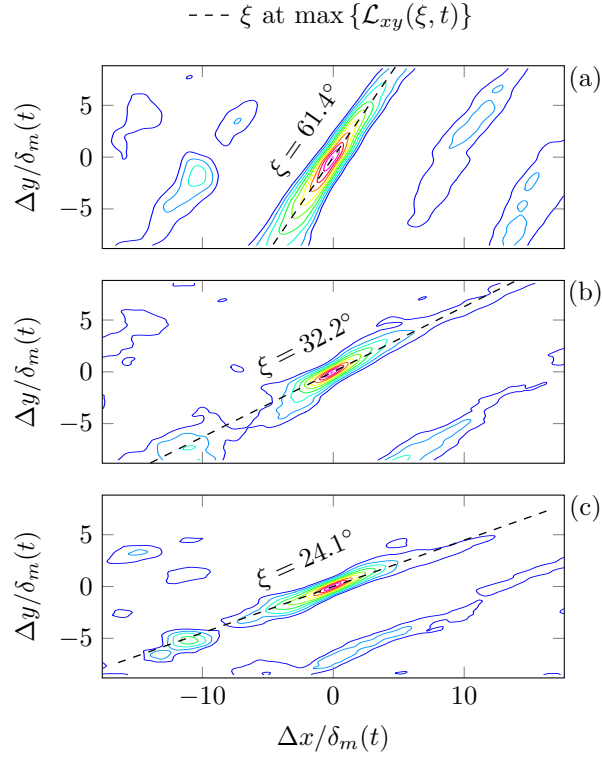


Figure 26: Space-space correlation contours of pressure at $y/\delta_m(t) = 15$ when $\delta_m(t)/\delta_m^o = 35$ for (a) $M = 1.5$, (b) 2.5, and (c) 3.5. The dashed line corresponds to the orientation with respect the horizontal axis of the maximum integral length scale of the two-dimensional correlation function.

5.2 Results

For the DNS of $M = 0.9$ and $M = 2.5$, the skewness and variance budgets of pressure are computed. First, it is important to assess our approximation of the time rate-of-change of variance and skewness. A first-order approximation of the derivative of variance is given by

$$\frac{\partial \overline{(p')^2}}{\partial t} \approx \frac{\overline{(p')^2(t + \Delta t)} - \overline{(p')^2(t)}}{\Delta t}, \quad (34)$$

where the pressure field $p'(t + \Delta t)$ is evaluated using the standard fourth-order Runge-Kutta by solving

the entire compressible Navier-Stokes equations at a future time of $t + \Delta t$. The same approach is used for the skewness. Figure 27 shows the first-order error of approximating the variance and skewness temporal derivatives at the centerline ($y = 0$). As the time step is reduced, the approximation follows the expected -1 slope but then diverges due to round-off errors associated with evaluating the full equations at time steps that are numerically very close. A $\Delta t = 10^{-5}$ is used to approximate the rate of change of variance and skewness.

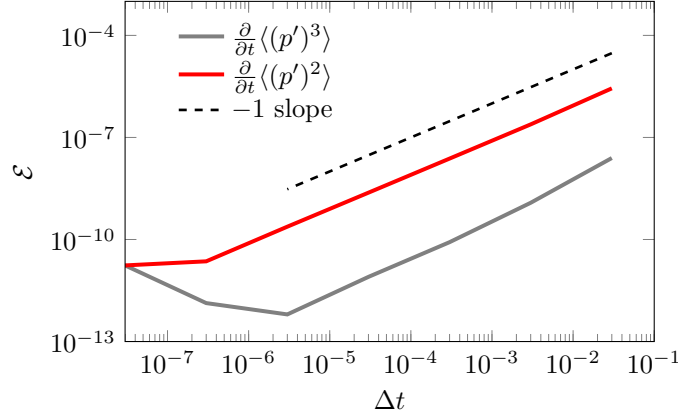


Figure 27: Error in first-order approximation of time rate-of-change of variance and skewness.

Figures 28 and 29 show the pressure variance budget for different y locations in the near acoustic field as a function of time for $M = 2.5$ and 0.9 , respectively. The statistics were averaged at the $\pm y$. The time traces of the components of the budget show how the initial transitioning shear layer radiates sound for $t \lesssim 100$. For both cases, the pressure-dilation term makes up most of the acoustic distribution. For the $M = 2.5$ case, the entropic contribution is slightly larger than the $M = 0.9$ which is expected since at $M = 2.5$ contain Mach-like waves which are weak shock-like features with steep gradients that can dissipate energy. For each y location the time rate-of-change of variance in the time average sense is larger than zero. This suggests that the intensity grows with time which is expected to occur for a growing shear layer whose volume increases with time meaning it will radiate more sound.

Figures 30 and 31 show the pressure skewness budget for different y locations in the near acoustic field as a function of time for $M = 2.5$ and 0.9 , respectively. For each y location the time rate-of-change of skewness in the time average sense is nearly zero. This suggests that as the shear layer grows the normalized skewness will remain constant.

6 Conclusions

DNS of high-speed turbulent shear layers for $M = 0.9, 1.5, 2.5$, and 3.5 have been completed. Analysis of acoustics show near-field nonlinearity of wave merging and flattening in the near acoustic field are important for skewness. Analysis of the skewness budget suggests that acoustic interaction effects are balanced by entropic contributions. This means the initial footprint of skewness must arise near the turbulence source. Skewness variation with distance from the shear layer supports this claim.

7 Personnel supported during duration of grant

The work is being supervised by Prof. Freund at UIUC. Funding supported the PhD studies Mr. Aaron Anderson and Mr. David Buchta.

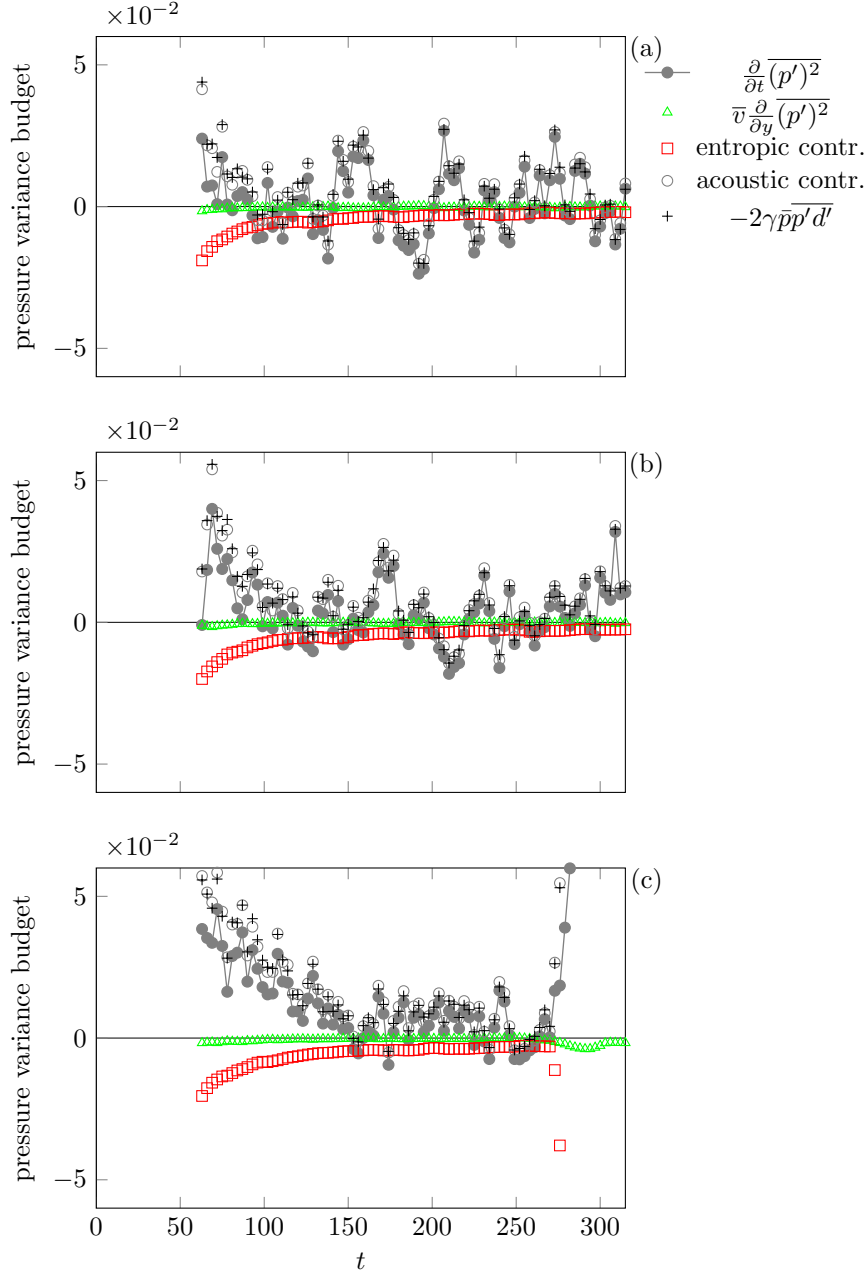


Figure 28: Budget of pressure variance for $M = 2.5$ at $y/\delta_m(t) = 7.5$ (a), 10 (b), and 15 (c). All components have been normalized by $\overline{(p')^2}$.

8 AFOSR point of contact

9 Publications

1. D. Buchta, J. B. Freund, "Near-field nonlinear interactions leading to jet crackle," Bulletin of the American Physical Society, San Francisco, CA (2014).
2. D. Buchta, A. Anderson, J. B. Freund, "Near-field shocks radiated by high-speed free-shear-flow turbulence," AIAA paper 2014-3201, Atlanta, GA (2014).
3. D. Buchta, J. B. Freund, "Jet crackle: near-field nonlinear acoustic interactions due to high-speed turbulent sources," Bulletin of the American Physical Society, Pittsburgh, PA (2013).

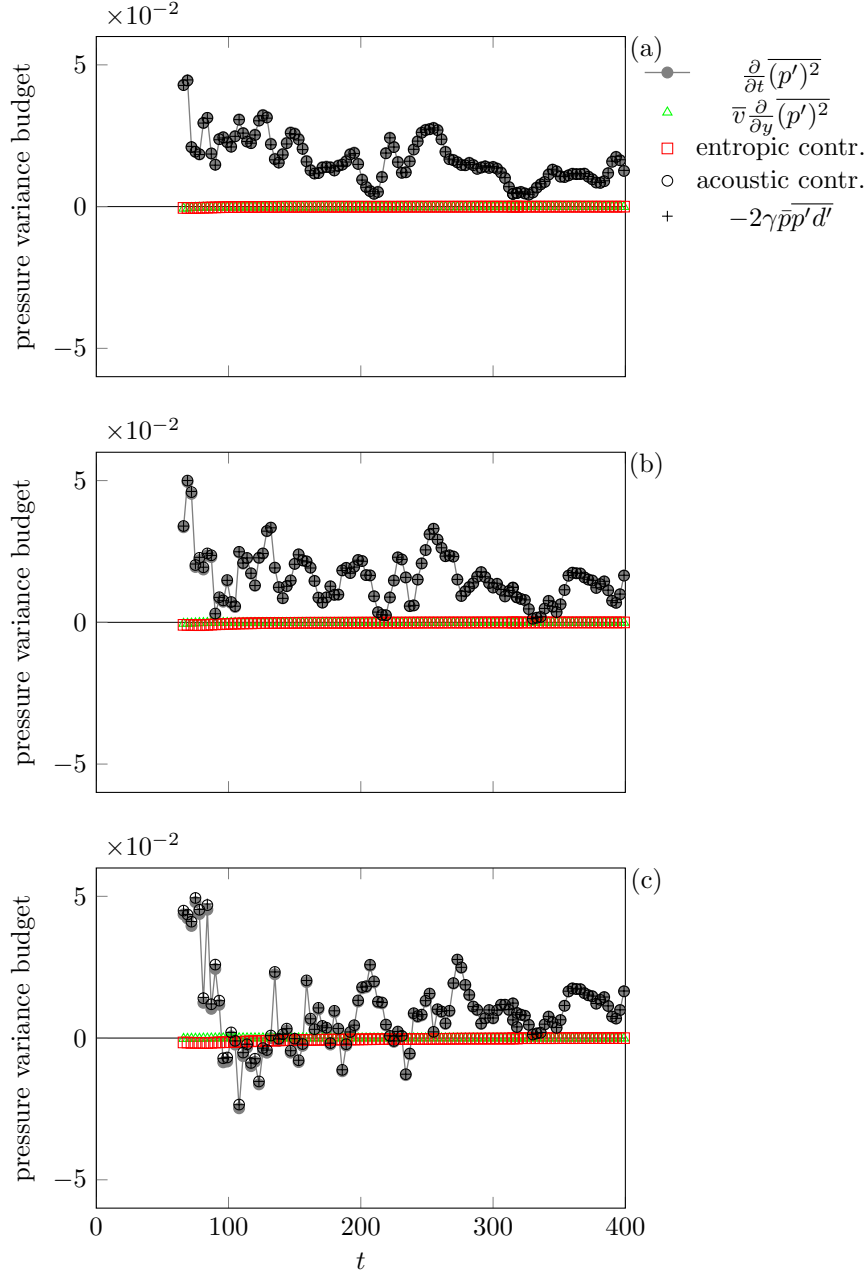


Figure 29: Budget of pressure variance for $M = 0.9$ at $y/\delta_m(t) = 7.5$ (a), 10 (b), and 15 (c). All components have been normalized by $\overline{(p')^2}$.

4. A. Anderson, J. B. Freund, "Source mechanisms of jet crackle," AIAA paper 2012-2251, Colorado Springs, CO (2012).
5. A. Anderson, J. B. Freund, "Mechanisms of 'crackle' acoustic radiation from high speed turbulence," Bulletin of the American Physical Society, San Diego, CA (2012).

10 Acknowledgment/disclaimer

This work was sponsored by the Air Force Office of Scientific Research, USAF, under grant number FA9550-10-1-0432. The views and conclusions contained herein are those of the authors and should

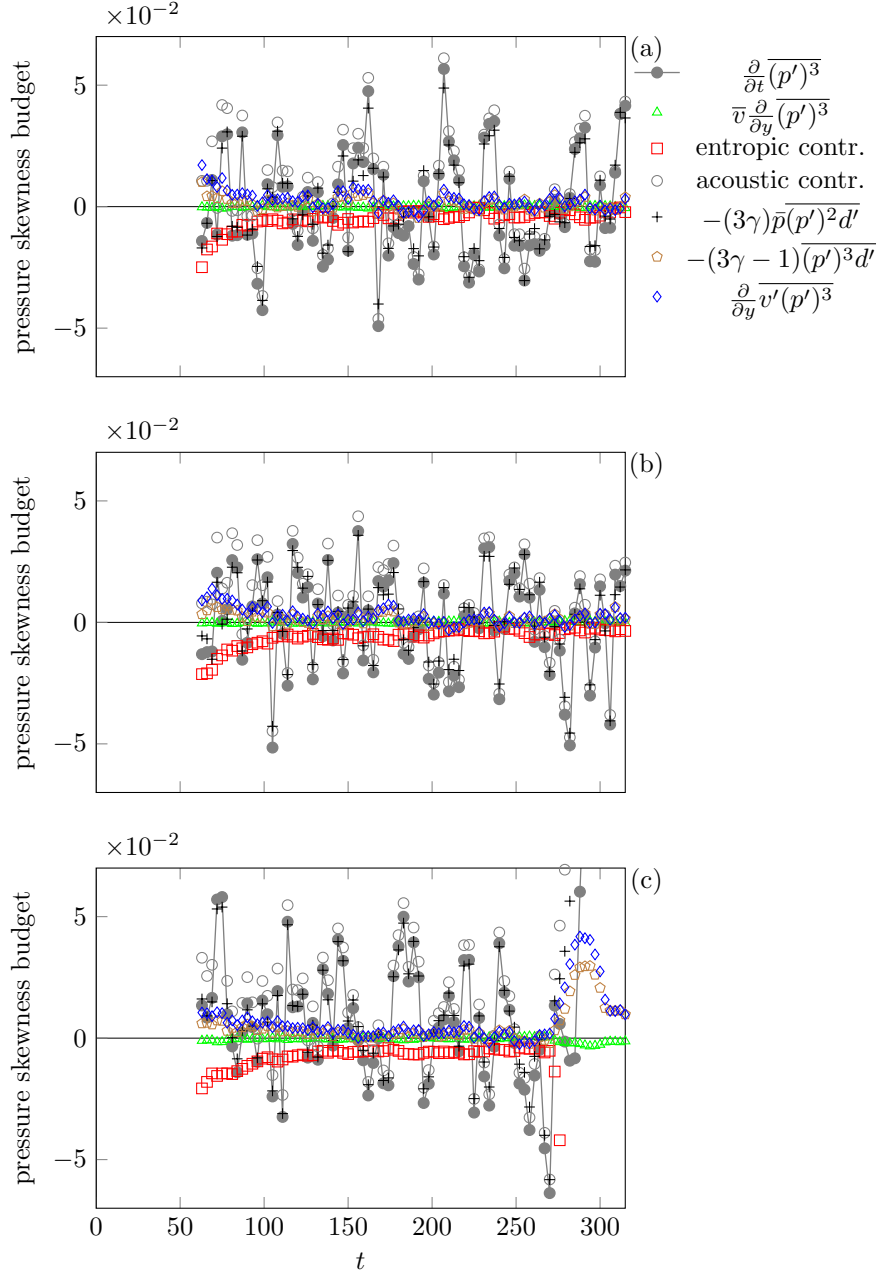


Figure 30: Budget of pressure skewness for $M = 2.5$ at $y/\delta_m(t) = 7.5$ (a), 10 (b), and 15 (c). All components have been normalized by $\overline{(p')^2}^{3/2}$.

not be interpreted as necessarily representing the official policies or endorsements, either expressed or implied, of the Air Force Office of Scientific Research or the U.S. Government.

A Flow equations

The nondimensional independent variables of space and time are

$$x = \frac{x^*}{l^*}, \quad y = \frac{y^*}{l^*}, \quad z = \frac{z^*}{l^*}, \quad t = \frac{t^* c_\infty^*}{l^*} \quad (35)$$

and the flow variables have been nondimensionalized by

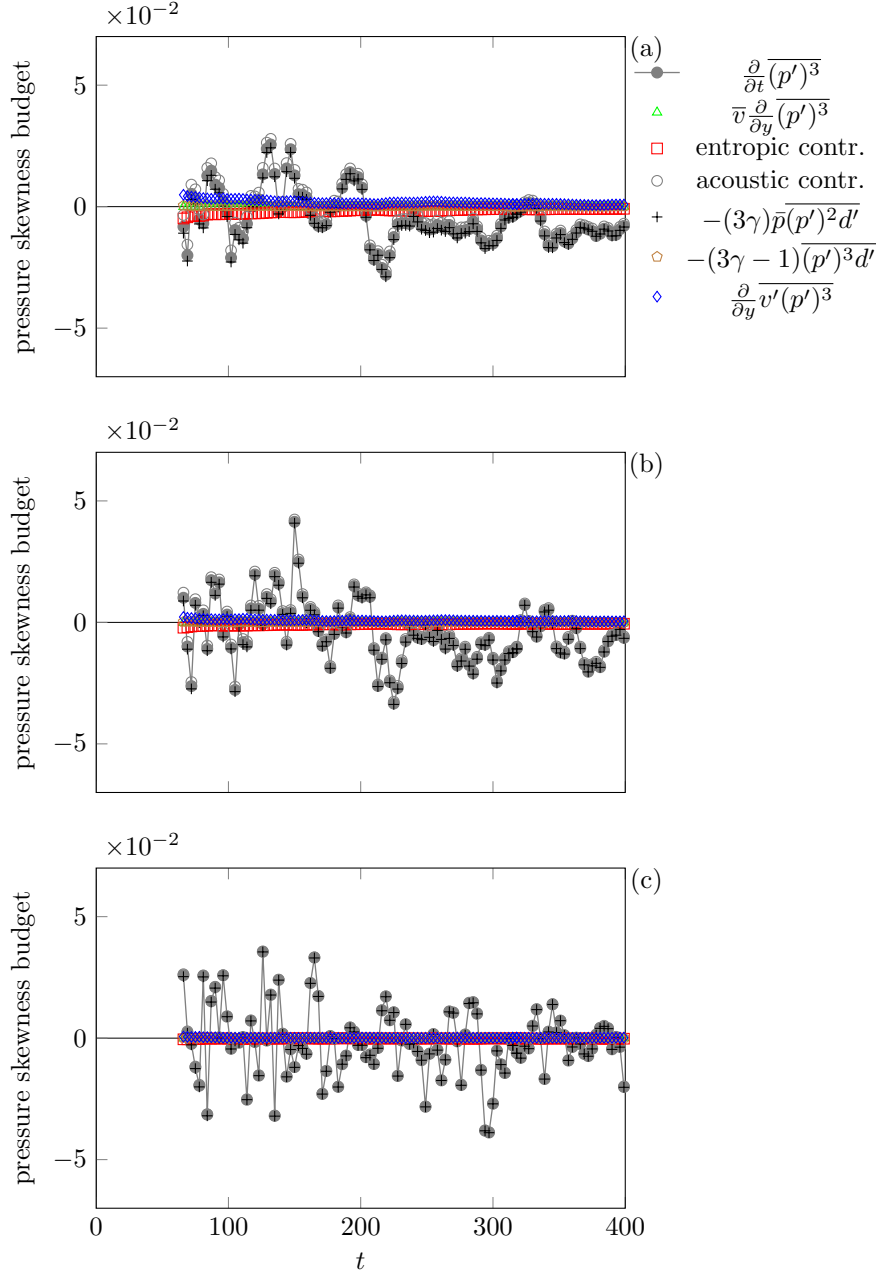


Figure 31: Budget of pressure skewness for $M = 0.9$ at $y/\delta_m(t) = 7.5$ (a), 10 (b), and 15 (c). All components have been normalized by $\overline{(p')^2}^{3/2}$.

$$\rho = \frac{\rho^*}{\rho_\infty^*}, \quad u_i = \frac{u_i^*}{c_\infty^*}, \quad T = \frac{T^* c_p^*}{(c_\infty^*)^2}, \quad p = \frac{p^*}{\rho_\infty^* (c_\infty^*)^2}. \quad (36)$$

The $()^*$ quantities represent dimensional ones and the freestream values of density, pressure, and speed of sound are denoted by ρ_∞ , p_∞ , and c_∞ , respectively. The specific heat at constant pressure is c_p . With the nondimensionalization given above, the compressible flow equations of mass, momentum, and energy are

$$\frac{\partial \rho}{\partial t} + \frac{\partial(\rho u_i)}{\partial x_i} = 0, \quad (37)$$

$$\frac{\partial(\rho u_i)}{\partial t} + \frac{\partial}{\partial x_i}(\rho u_i u_j) = -\frac{\partial p}{\partial x_i} + \frac{\partial \tau_{ij}}{\partial x_i}, \quad (38)$$

$$\frac{\partial e}{\partial t} + \frac{\partial}{\partial x_i} [u_i(e + p)] = -\frac{\gamma}{RePr(\gamma - 1)} \frac{\partial^2}{\partial x_i^2} \left(\frac{p}{\rho} \right) + \frac{\partial}{\partial x_i} (\tau_{ij} u_j), \quad (39)$$

respectively. The viscous stress tensor assuming a Newtonian fluid and neglecting the effect of bulk viscosity is expressed

$$\tau_{ij} = \frac{1}{Re} \left(\frac{\partial u_i}{\partial x_j} + \frac{\partial u_j}{\partial x_i} - \frac{2}{3} \frac{\partial u_k}{\partial x_k} \delta_{ij} \right), \quad (40)$$

The total energy assuming an ideal gas law is

$$e = \frac{p}{\gamma - 1} + \frac{1}{2} \rho u_i u_i. \quad (41)$$

The flow equations are parameterized by the ratio of specific heats, Reynolds number, Prandtl number given by

$$\gamma \equiv \frac{c_p^*}{c_v^*} = 1.4 \quad (42)$$

$$Re = \frac{\rho_\infty^* c_\infty^* l^*}{\mu^*} \quad (43)$$

$$Pr \equiv \frac{c_p^* \mu^*}{\kappa^*} = 0.7. \quad (44)$$

The dynamic viscosity (μ^*) and thermal conductivity (κ^*) are assumed constant. The Reynolds number can be rescaled to reflect a more useful comparison between flows of different speed. The Reynolds number based on the momentum thickness and velocity difference is written as

$$Re_{\delta_m} = \frac{\rho_\infty \Delta U^* \delta_m^*(t)}{\mu^*} \quad (45)$$

The relationship between the simulation Reynolds number and momentum thickness Reynolds number is

$$Re_{\delta_m} = Re M \delta_m^*(t) / l^*, \quad (46)$$

where the Mach number is

$$M = \frac{\Delta U^*}{c_\infty^*}. \quad (47)$$

B Numerics

B.1 Discrete Fourier method

The discrete Fourier transform of a periodic function f represented by N uniformly spaced grid points is

$$\hat{f}(k_j) = \frac{1}{N} \sum_{m=0}^{N-1} f(x_m) \exp(-\sqrt{-1} k_j x_m), \quad (48)$$

where x_m is the spatial location at the m^{th} -grid point and the wavenumber is defined as

$$k_l = \frac{2\pi l}{N \Delta x}. \quad (49)$$

The discrete inverse Fourier transform is given as

$$f(x_j) = \sum_{m=N/2}^{N/2-1} \hat{f}(k_m) \exp(\sqrt{-1}k_m x_j), \quad (50)$$

and the first and second order derivatives can be written as

$$f'(x_j) = \sum_{m=N/2}^{N/2-1} \sqrt{-1}k_m \hat{f}(k_m) \exp(\sqrt{-1}k_m x_j) \text{ and} \quad (51)$$

$$f''(x_j) = \sum_{m=N/2}^{N/2-1} -k_m^2 \hat{f}(k_m) \exp(\sqrt{-1}k_m x_j), \quad (52)$$

respectively.

B.2 Finite difference first derivative

The approximation of the first derivative at spatial location x_o can be written as

$$\frac{\partial}{\partial x} f(x_o) \approx \sum_{i=-M}^M b_i f'(x_o + i\Delta x) = \frac{1}{\Delta x} \sum_{j=-N}^N a_j f(x_o + j\Delta x), \quad (53)$$

where the coefficients are assumed to have symmetry $b_i = b_{-i}$ and $a_i = -a_{-i}$. Traditionally (Lele, 1992), the coefficients are determined by matching terms in the Taylor series substituted in equation 53. Others (Tam & Webb, 1993; Bogey & Bailly, 2004) have used a combined approach to determine the coefficients. The truncated Taylor series approximation is used to enforce a desired order of accuracy, and the remaining coefficients are determined by minimizing the error between the exact and approximate dispersion relation. The properties of the scheme then preserve aspects of the dispersion properties of the derivative. For an explicit ($M = 0$) 7-point stencil ($N = 3$) each of the terms in finite difference expression is written as a Taylor series expansion up to $O(\Delta x^6)$ by

$$\begin{aligned} f_{j+1} &\sim f_j + f'_j \Delta x + \frac{f''_j}{2!} (\Delta x)^2 + \frac{f'''_j}{3!} (\Delta x)^3 + \frac{f^{(4)}_j}{4!} (\Delta x)^4 + \frac{f^{(5)}_j}{5!} (\Delta x)^5 + \dots \\ f_{j-1} &\sim f_j - f'_j \Delta x + \frac{f''_j}{2!} (\Delta x)^2 - \frac{f'''_j}{3!} (\Delta x)^3 + \frac{f^{(4)}_j}{4!} (\Delta x)^4 - \frac{f^{(5)}_j}{5!} (\Delta x)^5 + \dots \\ f_{j+2} &\sim f_j + f'_j 2\Delta x + \frac{f''_j}{2!} (2\Delta x)^2 + \frac{f'''_j}{3!} (2\Delta x)^3 + \frac{f^{(4)}_j}{4!} (2\Delta x)^4 + \frac{f^{(5)}_j}{5!} (2\Delta x)^5 + \dots \\ f_{j-2} &\sim f_j - f'_j 2\Delta x + \frac{f''_j}{2!} (2\Delta x)^2 - \frac{f'''_j}{3!} (2\Delta x)^3 + \frac{f^{(4)}_j}{4!} (2\Delta x)^4 - \frac{f^{(5)}_j}{5!} (2\Delta x)^5 + \dots \\ f_{j+3} &\sim f_j + f'_j 3\Delta x + \frac{f''_j}{2!} (3\Delta x)^2 + \frac{f'''_j}{3!} (3\Delta x)^3 + \frac{f^{(4)}_j}{4!} (3\Delta x)^4 + \frac{f^{(5)}_j}{5!} (3\Delta x)^5 + \dots \\ f_{j-3} &\sim f_j - f'_j 3\Delta x + \frac{f''_j}{2!} (3\Delta x)^2 - \frac{f'''_j}{3!} (3\Delta x)^3 + \frac{f^{(4)}_j}{4!} (3\Delta x)^4 - \frac{f^{(5)}_j}{5!} (3\Delta x)^5 + \dots \end{aligned}$$

Substituting these relations into the differencing equation and matching like terms, the constraint equations that enforce formal order of accuracy up to sixth order are

$$a_0 = 0 \quad (54)$$

$$2a_1 + 4a_2 + 6a_3 = 1 \text{ (second order)} \quad (55)$$

$$\frac{2}{3!}a_1 + \frac{2 \cdot 2^3}{3!}a_2 + \frac{2 \cdot 3^3}{3!}a_3 = 0 \text{ (fourth order)} \quad (56)$$

$$\frac{2}{5!}a_1 + \frac{2 \cdot 2^5}{5!}a_2 + \frac{2 \cdot 3^5}{5!}a_3 = 0 \text{ (sixth order)}. \quad (57)$$

Directly solving of equations 55-57 results the standard sixth-order approximation with coefficients

$$\begin{aligned} a_0 &= 0 \\ a_1 &= -a_{-1} = 0.7500000000000000 \\ a_2 &= -a_{-2} = -.1500000000000000 \\ a_3 &= -a_{-3} = 0.0166666666666667. \end{aligned}$$

Up to this point, there has been no guarantee that the finite-difference approximation mimics the properties of the first derivative in wavenumber space. To obtain a resolution-optimized fourth-order method for example, relations 55 and 56 are enforced leaving one free-parameter to be tuned. The tuning scheme involves an optimization in Fourier space. The scheme can be written in Fourier space by substituting the inverse discrete Fourier transform (equation 50). Ignoring the summation over the modes the differencing approximation is

$$\sum_{i=-M}^M b_i \sqrt{-1} k \hat{f}(k) \exp[\sqrt{-1} k(x + i\Delta x)] = \frac{1}{\Delta x} \sum_{j=-N}^N a_j \hat{f}(k) \exp[\sqrt{-1} k(x + j\Delta x)], \quad (58)$$

and cancelling $\hat{f}(k) \exp[\sqrt{-1} k(x)]$ from both sides we have

$$\sum_{i=-M}^M b_i \sqrt{-1} k \exp[\sqrt{-1} k(i\Delta x)] = \frac{1}{\Delta x} \sum_{j=-N}^N a_j \exp[\sqrt{-1} k(j\Delta x)]. \quad (59)$$

Isolating $k\Delta x$ on the left-hand-side

$$k\Delta x = \frac{-\sqrt{-1} \sum_{j=-N}^N a_j \exp[\sqrt{-1} k(j\Delta x)]}{\sum_{i=-M}^M b_i \exp[\sqrt{-1} k(i\Delta x)]} \quad (60)$$

and recalling Euler's formula

$$\begin{aligned} \cos(x) &= \frac{\exp(\sqrt{-1}x) + \exp(-\sqrt{-1}x)}{2} \\ \sin(x) &= \frac{\exp(\sqrt{-1}x) - \exp(-\sqrt{-1}x)}{2\sqrt{-1}} \end{aligned}$$

the effective wavenumber equation is

$$(k\Delta x)' = \frac{2 \sum_{j=1}^N a_j \sin(jk\Delta x)}{b_o + 2 \sum_{i=1}^M b_i \cos(ik\Delta x)}. \quad (61)$$

The explicit finite-difference ($M = 0$) equation approximates the first derivative as a truncated sine series in Fourier space. A real-valued expression for equation 61 is a consequence that the coefficients were symmetric; otherwise the dispersion relation would be complex. The $(k\Delta x)'$ notation in equation 61 denotes an approximation to the exact wavenumber relation $(k\Delta x)$.

To preserve aspects of the actual dispersion relation, the integral error,

$$E = \int_{\ln(a)}^{\ln(b)} [(k\Delta x) - (k\Delta x)']^2 d \ln(k\Delta x), \quad (62)$$

between the exact and effective wavenumber will be minimized to obtain a final relation to solve the final tuning parameter. The limits of integration for a seven-point $M = 3$ scheme is $a = \pi/16$ and $b = \pi/2$.

The thirteen-point schemes uses $a = \pi/16$ and $b = 3\pi/5$. For the fourth-order $M = 3$ scheme, the final constraint that optimizes the integral error is

$$\frac{\partial E}{\partial a_3} = 0. \quad (63)$$

Figure 33 shows the effective wavenumber and associated error with respect to the exact relation. By sacrificing order of accuracy for resolution, the optimized formulas (abbreviated opt.) have more error in the low-wavenumber range. The standard schemes (abbreviated std.) have coefficients that maximize formal order of accuracy. For the seven-point $M = 3$, fourth-order resolution optimized scheme the coefficients are

$$\begin{aligned} a_0 &= 0 \\ a_1 &= -a_{-1} = 0.824639848382100 \\ a_2 &= -a_{-2} = -0.209711878705680 \\ a_3 &= -a_{-3} = 0.0315946363430865 \end{aligned}$$

The coefficients for the $M = 6$, fourth-order scheme are

$$\begin{aligned} a_0 &= 0 \\ a_1 &= -a_{-1} = 0.9108405208695360 \\ a_2 &= -a_{-2} = -0.3419538377082619 \\ a_3 &= -a_{-3} = 0.1380399894807369 \\ a_4 &= -a_{-4} = -0.04827039810294327 \\ a_5 &= -a_{-5} = 0.008624243759248696 \\ a_6 &= -a_{-6} = -0.0006681390707308727. \end{aligned}$$

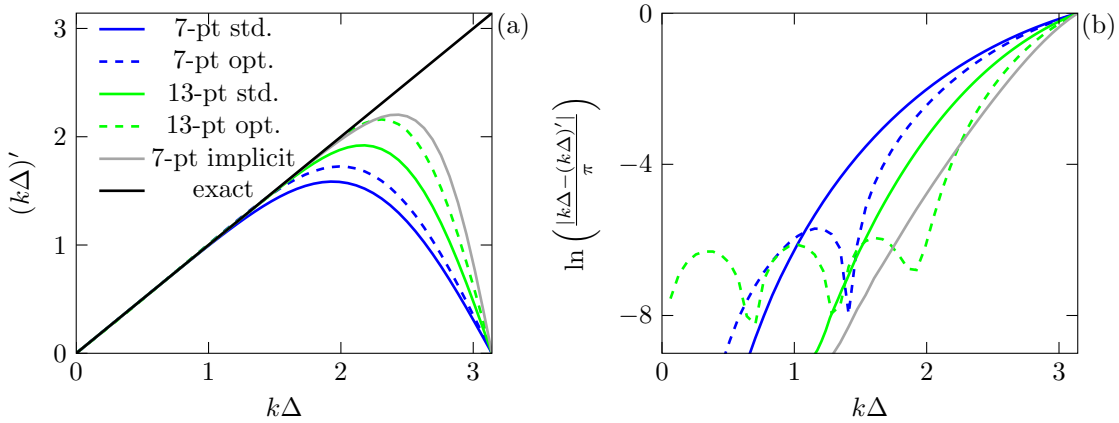


Figure 32: Effective wavenumber of the interior first derivative (a) and associated difference from the exact (b).

Near-boundary points use reduced-order central differences as described in Freund (1997a). On the boundaries a third-order one-sided approximation is used.

B.3 Finite difference second derivative

The explicit finite difference approximation of the second derivative is given by

$$\frac{\partial^2}{\partial x^2} f(x_o) \approx f''(x_o) = \frac{1}{(\Delta x)^2} \sum_{j=-N}^N c_j f(x_o + j\Delta x), \quad (64)$$

with constraint equations for $N = 3$ on coefficients enforcing formal order of accuracy up to sixth-order by

$$c_0 + 2c_1 + 2c_2 + 2c_3 = 0 \quad (65)$$

$$\frac{2}{2!}c_1 + \frac{2 \cdot 2^2}{2!}c_2 + \frac{2 \cdot 3^2}{2!}c_3 = 1 \text{ (second order)} \quad (66)$$

$$\frac{2}{4!}c_1 + \frac{2 \cdot 2^4}{4!}c_2 + \frac{2 \cdot 3^4}{4!}c_3 = 0 \text{ (fourth order)} \quad (67)$$

$$\frac{2}{6!}c_1 + \frac{2 \cdot 2^6}{6!}c_2 + \frac{2 \cdot 3^6}{6!}c_3 = 0 \text{ (sixth order)}. \quad (68)$$

$$(69)$$

Directly solving equations 65-68 results in the standard sixth-order scheme with coefficients

$$\begin{aligned} c_0 &= -2.72222222222222 \\ c_1 &= c_{-1} = 1.50000000000000 \\ c_2 &= c_{-2} = -.150000000000000 \\ c_3 &= c_{-3} = 0.0111111111111111. \end{aligned}$$

Substituting the discrete Fourier representation of the function in equation 72, a modified wavenumber expression for the explicit finite-difference approximation of the second derivative is

$$(k\Delta x)'' = c_0 + 2 \sum_{j=1}^N c_j \cos(j\Delta x). \quad (70)$$

The modified wave number approximates the exact dispersion relation by a truncated cosine series. The square error between the exact and effective wavenumber on a scaled periodic domain $[0, \pi)$ is given by

$$E = \int_{\ln(a)}^{\ln(b)} [(k\Delta x)^2 - (k\Delta x)'']^2 d \ln(k\Delta x), \quad (71)$$

where the bounds of integration for a seven-point scheme are $a = \pi/16$ and $b = \pi/2$. For a thirteen-point scheme $a = \pi/16$ and $b = 3\pi/5$. Figure 33 gives the modified wave number and error associated with seven-point and thirteen-point schemes of the second derivative. Like the first derivative, the optimized methods, by sacrificing maximum accuracy for resolution, lower wavenumbers are increased error.

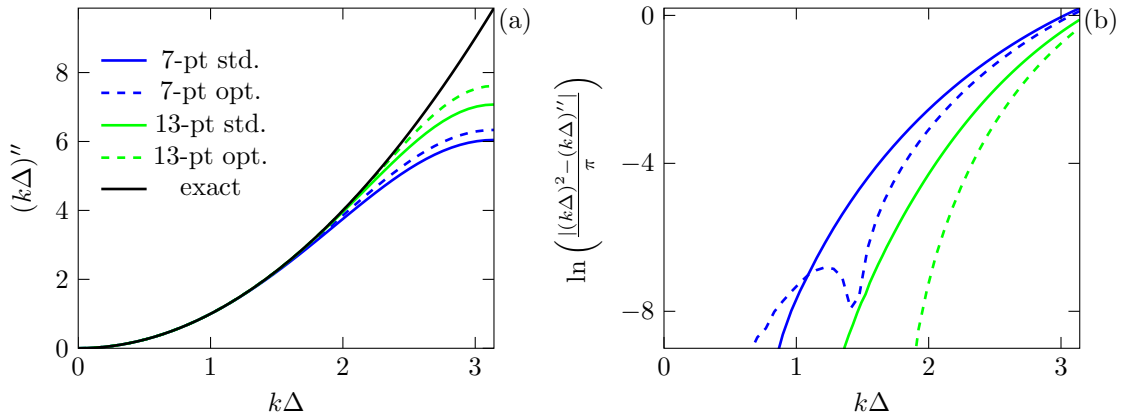


Figure 33: Effective wavenumber of the interior second derivative (a) and associated difference from the exact (b).

The coefficients for the resolution optimized $M = 3$ and 6 schemes are

$$\begin{aligned}
c_0 &= -2.81321312844389 \\
c_1 &= c_{-1} = 1.56824317966625 \\
c_2 &= c_2 = -.177297271866500 \\
c_3 &= c_3 = 0.0156606564221945.
\end{aligned}$$

$$\begin{aligned}
c_0 &= -3.093268941798102 \\
c_1 &= c_{-1} = 1.811759211319885 \\
c_2 &= c_2 = -.3343827021872651 \\
c_3 &= c_3 = 0.08734940331848545 \\
c_4 &= c_4 = -0.02186933368500581 \\
c_5 &= c_5 = 0.004224346387577600 \\
c_6 &= c_6 = -0.0004464542546261400.
\end{aligned}$$

respectively. Near-boundary points use reduced-order central differences. For $i = 2$, $i = N - 2$, a standard fourth-order method is used with coefficients

$$\begin{aligned}
c_0 &= -2 \\
c_1 &= a_{-1} = 1 \\
&\cdot
\end{aligned}$$

For $i = 1$, $i = N - 1$, second-order scheme is used with coefficients

$$\begin{aligned}
c_0 &= \frac{-5}{2} \\
c_1 &= c_{-1} = \frac{4}{3} \\
c_2 &= c_{-2} = -\frac{1}{12} \\
&\cdot
\end{aligned}$$

On the boundaries, a one-sided, third-order method is used where the coefficients at $i = 1$ are given by

$$\begin{aligned}
c_0 &= 2 \\
c_1 &= -5 \\
c_2 &= 4 \\
c_2 &= -1 \\
&\cdot
\end{aligned}$$

B.4 Selective high-wave number filtering

It may be necessary to apply a selective high-wave number filtering to the solution so that parasitic, short wavelength waves do not deteriorate the solution. The differencing equation is similar to Bogey & Bailly (2004) given here as

$$\tilde{f}(x_o) = f(x_o) - \sum_{j=-N}^N h_j f(x_o + j\Delta x). \quad (72)$$

For a thirteen-point ($N = 6$) scheme and assuming $h_i = h_{-1}$, the constraint equations of formal order of accuracy are written

$$1 - (h_o + 2h_1 + 2h_2 + 2h_3 + 2h_4 + 2h_5 + 2h_6) = 1 \quad (73)$$

$$- \left(\frac{2}{2!}h_1 + \frac{2 \cdot 2^2}{2!}h_2 + \frac{2 \cdot 3^2}{2!}h_3 + \frac{2 \cdot 4^2}{2!}h_4 + \frac{2 \cdot 5^2}{2!}h_5 + \frac{2 \cdot 6^2}{2!}h_6 \right) = 0 \text{ (second order)} \quad (74)$$

$$- \left(\frac{2}{4!}h_1 + \frac{2 \cdot 2^4}{4!}h_2 + \frac{2 \cdot 3^4}{4!}h_3 + \frac{2 \cdot 4^4}{4!}h_4 + \frac{2 \cdot 5^4}{4!}h_5 + \frac{2 \cdot 6^4}{4!}h_6 \right) = 0 \text{ (fourth order)} \quad (75)$$

$$- \left(\frac{2}{6!}h_1 + \frac{2 \cdot 2^6}{6!}h_2 + \frac{2 \cdot 3^6}{6!}h_3 + \frac{2 \cdot 4^6}{6!}h_4 + \frac{2 \cdot 5^6}{6!}h_5 + \frac{2 \cdot 6^6}{6!}h_6 \right) = 0 \text{ (sixth order)} \quad (76)$$

$$- \left(\frac{2}{8!}h_1 + \frac{2 \cdot 2^8}{8!}h_2 + \frac{2 \cdot 3^8}{8!}h_3 + \frac{2 \cdot 4^6}{6!}h_4 + \frac{2 \cdot 5^6}{6!}h_5 + \frac{2 \cdot 6^6}{6!}h_6 \right) = 0 \text{ (eighth order)} \quad (77)$$

$$- \left(\frac{2}{10!}h_1 + \frac{2 \cdot 2^{10}}{10!}h_2 + \frac{2 \cdot 3^{10}}{10!}h_3 + \frac{2 \cdot 4^{10}}{10!}h_4 + \frac{2 \cdot 5^{10}}{10!}h_5 + \frac{2 \cdot 6^{10}}{10!}h_6 \right) = 0 \text{ (tenth order)} \quad (78)$$

$$- \left(\frac{2}{12!}h_1 + \frac{2 \cdot 2^{12}}{12!}h_2 + \frac{2 \cdot 3^{12}}{12!}h_3 + \frac{2 \cdot 4^{12}}{12!}h_4 + \frac{2 \cdot 5^{12}}{12!}h_5 + \frac{2 \cdot 6^{12}}{12!}h_6 \right) = 0 \text{ (twelfth order)}. \quad (79)$$

A transfer function in wavenumber space can be found, much like the modified wavenumbers of the derivative approximations. For the explicit formuals used here, the transfer function is

$$T(k\Delta) = 1 - \left(h_o + 2 \sum_{j=1}^N h_j \cos(j\Delta x) \right), \quad (80)$$

and the square integral error between the filtered and un-filtered solutions is

$$E = \int_{\ln(a)}^{\ln(b)} [1 - T(k\Delta x)]^2 d \ln(k\Delta x), \quad (81)$$

where the limits of integration for the seven-point are $a = \pi/16$ and $b = 3\pi/32$. For the thirteen-point formulas the limits are $a = \pi/16$ and $b = \pi/2$. The coefficients for the seven- and thirteen-point formulas by minimizing equation 81 are given as

$$\begin{aligned} h_0 &= 0.288090709024785 \\ h_1 &= h_{-1} = -0.228272677256196 \\ h_2 &= h_{-2} = 0.105954645487608 \\ h_3 &= h_{-3} = -0.02172732274380381 \end{aligned}$$

$$\begin{aligned} h_0 &= 0.1913963126291382 \\ h_1 &= h_{-1} = -0.1719104977994496 \\ h_2 &= h_{-2} = 0.1237396648728178 \\ h_3 &= h_{-3} = -0.06976715092480617 \\ h_4 &= h_{-4} = 0.02936617293645158 \\ h_5 &= h_{-5} = -0.008322351275744250 \\ h_6 &= h_{-6} = 0.001196005876161525 \end{aligned}$$

respectively.

When an implicit filtering scheme is desired, the finite difference equation can be written as

$$\sum_{i=-M}^M g_i \tilde{f}(x_o + i\Delta x) = \sum_{j=-N}^N h_j f(x_o + j\Delta x), \quad (82)$$

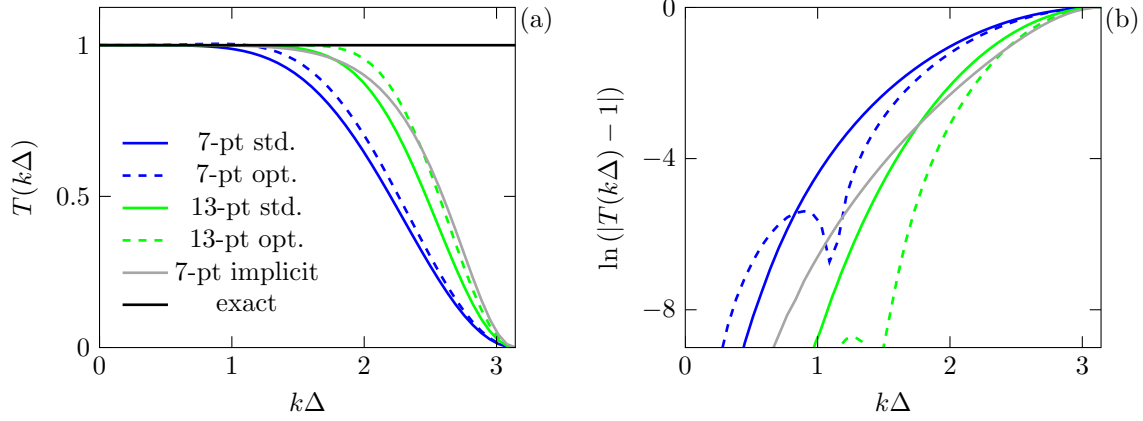


Figure 34: Transfer function of the interior high-wavenumber filter (a) and associated difference from the exact (b).

and the same process as described above for selecting the stencil width, formal order of accuracy, and enforcing an effective wavenumber behavior is carried out. Following Lele (1992), the resolution behavior in wavenumber space is set differently than Tam & Webb (1993); Bogey & Bailly (2004). Values of $T(k\Delta)$ at a particular $k\Delta$ to find the remaining degrees of freedom of the stencil formula. The behavior at $k\Delta = \pi$ is also set to

$$\frac{d^2 T(k\Delta)}{d^2 k\Delta}(\pi) = 0. \quad (83)$$

Though this approach does not minimize the integral square difference between the actual and effective wave number resolution, the resolution properties are well-known and have not had any negative effects on the solution. The trends for the seven-point implicit scheme (C.2.10.b) designed by Lele (1992) are given in figure 34.

C Reynolds number effect

A higher Reynolds number simulation at $Re_{\delta_m^o} = 120$ was run for $M = 2.5$. The grid in the x -, y - and z -directions was uniformly spaced with $\Delta x = \Delta y = \Delta z = 0.5\delta_m^o$ which is nearly two times the resolution of the $Re_{\delta_m^o} = 60$ simulations. The numerics of the high-Reynolds number simulation were modified. The first-order derivatives in all directions were computed with a 13-point, fourth-order resolution optimized scheme designed by Bogey & Bailly (2004). A 13-point fourth-order filter was applied every 5 time steps in all three coordinate directions. The second derivative was evaluated by repeated first-order derivatives. High-order, non-centered schemes crafted by Berland *et al.* (2007) were used for derivative approximations near boundaries.

An identical numerical scheme in all coordinate directions of equal spatial resolution tests the robustness of the initial numerical scheme. This verifies the sufficient resolution of the initial simulations and that any potentially negative anisotropic effects of the numerical method did not affect the statistics of interest.

D Instability modes of inviscid parallel temporal shear layers

The primitive flow variables are expressed by a Reynolds decomposition,

$$[u, v, w, \rho, T] = [\bar{u}, \bar{v}, \bar{w}, \bar{\rho}, \bar{T}] + [u', v', w', \rho', T'], \quad (84)$$

where $\bar{()}$ is an average in the statistically homogeneous directions and $()'$ represent a perturbation quantity. The mean flow quantities are prescribed by

$$[\bar{u}, \bar{v}, \bar{w}, \bar{\rho}, \bar{T}](y) = [u(y), 0, 0, 1, T(u)], \quad (85)$$

with small-amplitude (ϵ) perturbations in the form of travelling waves

$$[u', v', w', \rho', T'] = \epsilon \text{Re} \left([\hat{u}, \hat{v}, \hat{w}, \hat{\rho}, \hat{T}](y) \exp\{i(\alpha x + \beta z - \omega t)\} \right). \quad (86)$$

This same formulation has been described elsewhere (Sandham, 1989) and a brief outline will be explained here. Substituting the mean and perturbation quantities into the inviscid, compressible flow equations and neglecting quadrating interactions of perturbation quantities, a set of ordinary differential equations is given as

$$\hat{\rho}i(\alpha\bar{u} - \omega) + \hat{v}\frac{d\bar{\rho}}{dy} + \bar{\rho} \left[i(\alpha\hat{u} + \beta\hat{w}) + \frac{d\hat{v}}{dy} \right] = 0 \quad (87)$$

$$\bar{\rho} \left[i(\alpha\bar{u} - \omega)\hat{u} + \hat{v}\frac{d\bar{u}}{dy} \right] = \frac{-i\alpha\hat{p}}{\gamma M_1^2} \quad (88)$$

$$\bar{\rho} [i(\alpha\bar{u} - \omega)\hat{v}] = -\frac{d\hat{p}}{dy} \frac{1}{\gamma M_1^2} \quad (89)$$

$$\bar{\rho} [i(\alpha\bar{u} - \omega)\hat{w}] = \frac{-i\beta\hat{p}}{\gamma M_1^2} \quad (90)$$

$$\bar{\rho} \left[i(\alpha\bar{u} - \omega)\hat{T} + \hat{v}\frac{d\bar{T}}{dy} \right] = \quad (91)$$

$$-(\gamma - 1) \hat{p} = \left[i(\alpha\hat{u} + \beta\hat{w}) + \frac{d\hat{v}}{dy} \right] \bar{\rho}\hat{T} + \hat{\rho}\bar{T} \quad (92)$$

Using the method of Gropengiesser (1970), the equations can be combined to form two equations for \hat{v} and \hat{p} and then combined into a single eigenfunction in the form

$$\hat{\chi} = \frac{i\alpha\hat{p}}{\gamma M_1^2 \hat{v}}, \quad (93)$$

with evolution equation

$$\frac{d\hat{\chi}}{dy} = \frac{\alpha^2(\bar{u} - \omega/\alpha)}{\bar{T}} - \frac{\hat{\chi}(\hat{\chi}g + \frac{d\bar{u}}{dy})}{(\bar{u} - \omega/\alpha)}, \quad (94)$$

where

$$g = \frac{\alpha^2 + \beta^2}{\bar{\rho}\alpha^2} - \frac{M_1^2(\alpha\bar{u} - \omega)^2}{\alpha^2}. \quad (95)$$

By inspecting the behavior of the \hat{v} and \hat{p} eigenfunctions at $y \rightarrow \pm\infty$, the behavior of $\hat{\chi}$ is

$$\hat{\chi}(y = \pm\infty) = \frac{\alpha(\bar{u} - \omega/\alpha)}{\sqrt{g\bar{T}}}. \quad (96)$$

The mean velocity profile is set as

$$\bar{u} = \frac{\Delta U}{2} \tanh\left(\frac{1}{2\delta_m^o} y\right), \quad (97)$$

and the temperature relation is specified from the Crocco-Busemann relation assuming unity Prandtl number. For temporally developing shear layers, a real-valued mode (α, β) is specified with an initial

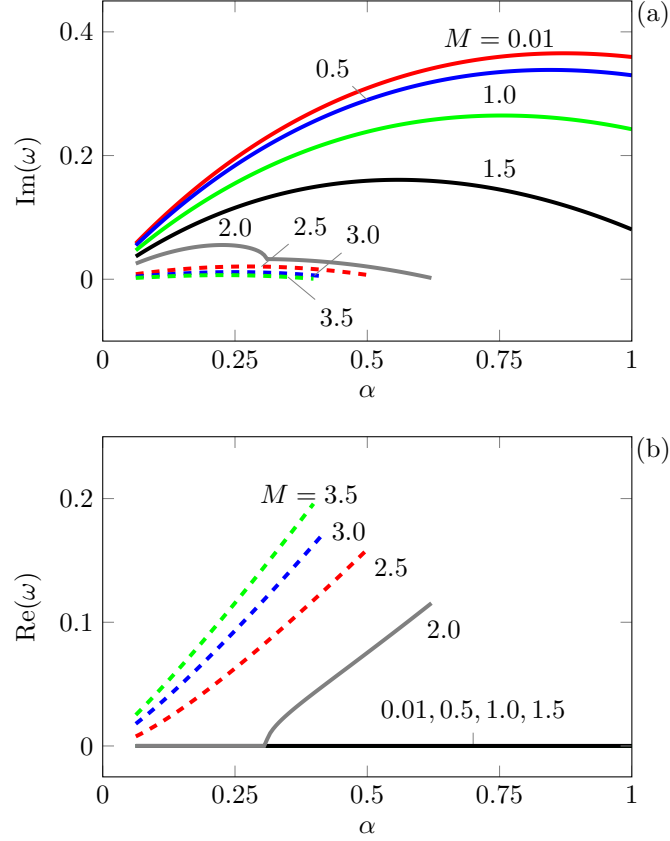


Figure 35: Variation of two-dimensional unstable modes with streamwise wavenumber, α : (a) temporal amplification rate and (b) rate of phase change.

guess of complex-valued ω . The evolution equation for $\hat{\chi}$ in equation (94) is integrated using a fifth-order adaptive-step-refinement Runge–Kutta scheme (Press *et al.*, 1986) from free-stream boundary conditions in equation (96) to the centerline at $y = 0$. The solutions at $y = 0$ from each of the free-stream conditions are compared and an update to the initial ω guess is made using a complex-valued Newton–Raphson method. Once the two values of $\hat{\chi}$ match at $y = 0$ to within specified tolerance of 10^{-14} , the procedure is stopped.

Figure 35 shows the solution of ω for two-dimensional, spanwise oriented modes $(\alpha, 0)$. As the Mach number increases, the amplification rate decreases. For $M_1 \gtrsim 2$, the phase speed of the mode is finite. These two-dimensional modes are known as the supersonic modes (Sandham, 1989), moving supersonic with respect to the free-stream velocity.

The behavior of three-dimensional amplification rate are shown in figure 36. As the Mach number increases, the amplification rate decreases. For $M \gtrsim 1.5$, the most amplified mode is three-dimensional, whereas for $M \lesssim 1$, the two-dimensional modes are the most amplified.

For $M = 0.9, 1.5, 2.5, 3.5$, the angle

$$\theta = \tan^{-1} \left(\frac{\beta}{\alpha} \right), \quad (98)$$

corresponding to the most unstable mode is given in figure 37. For $M_c \gtrsim 0.6$, the trend of the angle suggestively follows the relation

$$M_c \cos(\theta) = 0.6, \quad (99)$$

an observation from the stability calculations of Sandham & Reynolds (1990). The collapse of this data with M_c is rather robust to effects of varying velocity ratio, temperature ratio, and free-stream stagnation enthalpies (Sandham & Reynolds, 1990). For $M_c \gtrsim 0.6$, the Mach number normal to the unstable wave

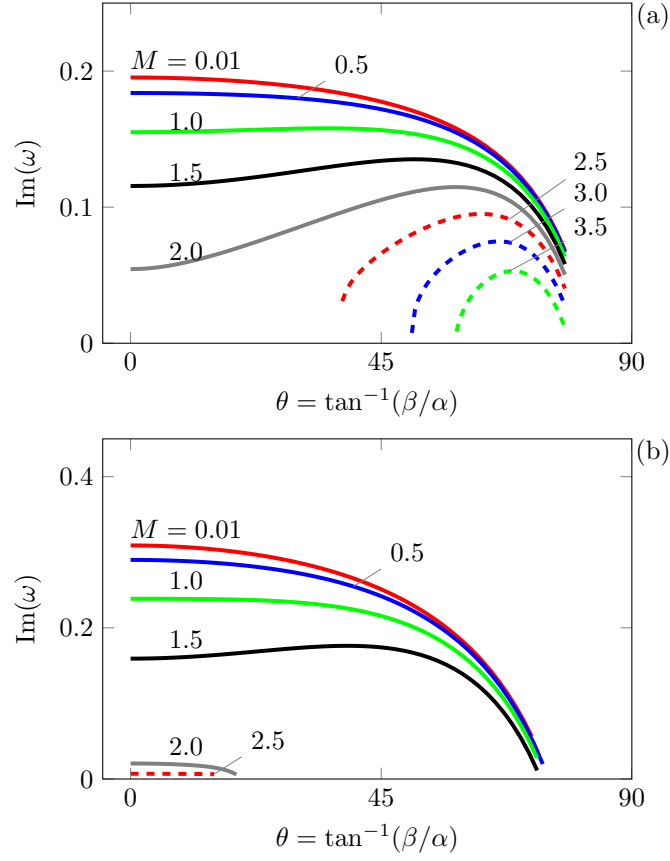


Figure 36: Variation of three-dimensional growth rates with angle between the streamwise and spanwise wavenumbers: (a) $\alpha = 0.25$ and (b) 0.5.

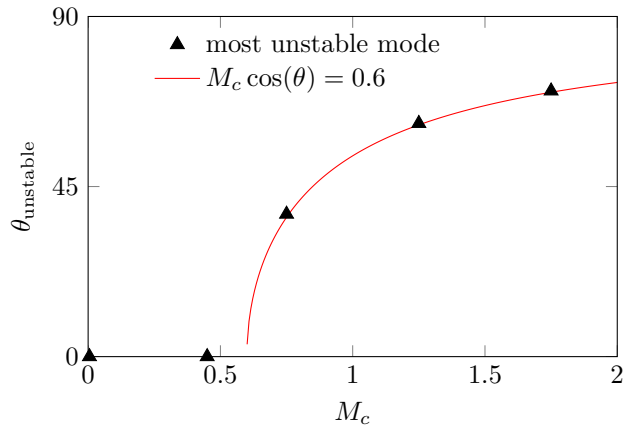


Figure 37: Angle of the most unstable three-dimensional mode with M_c . The line is an empirical relation given by Sandham & Reynolds (1990) for $M_c \gtrsim 0.6$.

crests is $M = 0.6$. From the perspective of the sonic eddy model of Breidenthal (1990) to participate in energy transfer processes, the subsonic speed normal to these waves that is predicted by linear theory suggests this is an important mechanism for instability of these shear layers at high speeds.

A connection can be made between the orientation of the wavefronts and the theoretical linear phase speed. The wavelength between wave crests in the y -direction (l_y) and the streamwise wavelength of the unstable mode ($l_x = 2\pi/k_x$) (shown in figure D) provides a measure of the orientation of the waves given by

$$\theta \equiv \tan^{-1} \left(\frac{l_y}{l_x} \right) = \tan^{-1} \left(\frac{17.87}{2\pi/0.289} \right) = 39.42^\circ. \quad (100)$$

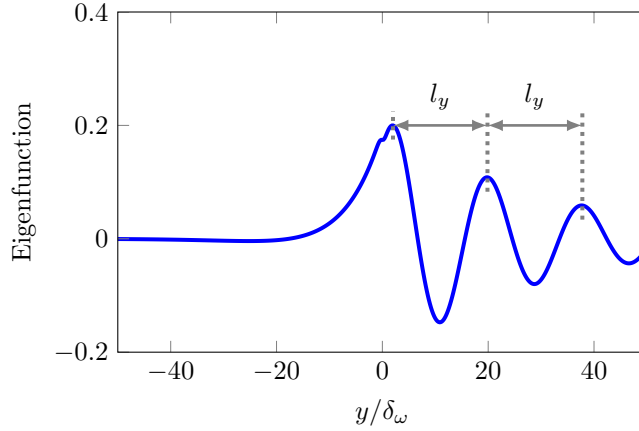


Figure 38: Schematic of radiating pressure eigenfunction for $M = 2.5$ with $k_x = 0.289$ and $l_y = 17.87$.

This direct measurement is compared to an inferred orientation based on the phase speed of the mode relative to the free-stream velocity. The phase speed is expressed as $c_m = Re(\omega)/\alpha = 0.259$. Given the non-dimensionalization of the disturbance equations this must be re-scaled by the free-stream Mach number $M = 1.25$ giving a velocity of 0.323. The wave angle is then

$$\theta_m = \sin^{-1} \left(\frac{1}{M_m} \right) = \sin^{-1} \left(\frac{c_\infty}{V_m + V_1} \right) = 39.46^\circ. \quad (101)$$

The agreement between the two approaches is promising; though, linear analysis overpredicts the wavefront orientation. For $M = 2.5$, DNS predicted an average angle of $\bar{\theta} = 34.2^\circ$ at $\delta_m(t)/\delta_m^o = 15$, suggesting structures are convecting faster than predicted by linear analysis. Empirical relations from Oertel (1979) suggests dominance of waves at an orientation of

$$\theta = \sin^{-1} \left(\frac{2}{1 + 2.5} \right) = 34.85^\circ, \quad (102)$$

assuming the equal free-stream sound speeds. This relation seems to correspond more closely to the observed orientation in the DNS data which may not be surprising since the Oertel (1979) relations are correlated to turbulent supersonic shear layers. Simulation by Nichols *et al.* (2013) have also shown qualitative agreement of wavefront orientation with using this relationship.

References

BAARS, W. J. & TINNEY, C. E. 2014 Shock-structures in the acoustic field of a Mach 3 jet with crackle. *Journal of Sound and Vibration* **333** (12), 2539 – 2553.

- BERLAND, JULIEN, BOGEY, CHRISTOPHE, MARSDEN, OLIVIER & BAILLY, CHRISTOPHE 2007 High-order, low dispersive and low dissipative explicit schemes for multiple-scale and boundary problems. *Journal of Computational Physics* **224** (2), 637 – 662.
- BOGEY, C. & BAILLY, C. 2004 A family of low dispersive and low dissipative explicit schemes for flow and noise computations. *Journal of Computational Physics* **194** (1), 194–214.
- BREIDENTHAL, ROBERT 1990 The sonic eddy - a model for compressible turbulence. In *28th Aerospace Sciences Meeting*. AIAA.
- CRIGHTON, D. G. 1986 Nonlinear acoustic propagation of broadband noise. In *Recent Advances in Aeroacoustics* (ed. Anjaneyulu Krothapalli & Charles A. Smith), pp. 411–454. Springer New York.
- DARKE, R. & FREUND, J. B. 2001 Mach wave radiation from a jet at Mach 1.92. *Physics of Fluids* **13** (9), S3.
- DEBISSCHOP, J. R., CHAMBRES, O. & BONNET, J. P. 1994 Velocity field characteristics in supersonic mixing layers. *Experimental Thermal and Fluid Science* **9** (2), 147–155.
- DUAN, LIAN, CHOUDHARI, MEELAN M. & WU, MINWEI 2014 Numerical study of acoustic radiation due to a supersonic turbulent boundary layer. *Journal of Fluid Mechanics* **746**, 165–192.
- ELLIOTT, G. S. & SAMIMY, M. 1990 Compressibility effects in free shear layers. *Physics of Fluids A: Fluid Dynamics (1989-1993)* **2** (7), 1231–1240.
- FFOWCS WILLIAMS, J. E. & MAIDANIK, G. 1965 The mach wave field radiated by supersonic turbulent shear flows. *Journal of Fluid Mechanics* **21**, 641–657.
- FFOWCS WILLIAMS, J. E., SIMSON, J. & VIRCHIS, V. J. 1975 ‘Crackle’: An annoying component of jet noise. *Journal of Fluid Mechanics* **71**, 251–271.
- FIÉVET, R., TINNEY, C. E. & BAARS, W. J. 2014 Acoustic waveforms produced by a laboratory scale supersonic jet. In *20th AIAA/CEAS Aeroacoustics Conference*. AIAA.
- FREUND, J. B. 1997*a* Compressibility effects in a turbulent annular mixing layer. PhD thesis, Stanford University.
- FREUND, J. B. 1997*b* Proposed inflow/outflow boundary condition for direct computation of aerodynamic sound. *AIAA Journal* **35** (4), 740–742.
- FREUND, J. B., LELE, S. K. & MOIN, P. 2000 Numerical simulation of a Mach 1.92 turbulent jet and its sound field. *AIAA Journal* **38** (11), 2023–2031.
- GEE, K. L., NEILSEN, T. B. & ATCHLEY, A. A. 2013 Skewness and shock formation in laboratory-scale supersonic jet data. *Journal of the Acoustical Society of America* **133** (6), 491–497.
- GEE, K. L., SPARROW, V. W., ATCHLEY, A. & GABRIELSON, T. B. 2007 On the perception of crackle in high-amplitude jet noise. *AIAA Journal* **45** (3), 593–598.
- GOEBEL, S. G. & DUTTON, J. C. 1991 Experimental study of compressible turbulent mixing layers. *AIAA journal* **29** (4), 538–546.
- GROPENGIESSER, H. 1970 Study on the stability of boundary layers and compressible fluids. *Tech. Rep.*. NASA TT F-12, 786.
- KLEINMAN, R. & FREUND, J. B. 2008 The sound from mixing layers simulated with different ranges of turbulence scales. *Physics of Fluids* **20** (10).
- KROTHAPALLI, A., ARAKERI, V. & GRESKA, B. 2003 Mach wave radiation: A review and an extension.
- KROTHAPALLI, A., VENKATAKRISHNAN, L. & LOURENCO, L. 2000 Crackle: A dominant component of supersonic jet mixing noise.

- LAUFER, J. 1961 Aerodynamic noise in supersonic wind tunnels. *Journal of the Aerospace Sciences* **28** (9), 685–692.
- LAUFER, J., SCHLINKER, R. & KAPLAN, R. E. 1976 Experiments on supersonic jet noise. *AIAA Journal* **14** (4), 489–497.
- LELE, S. K. 1992 Compact finite difference schemes with spectral-like resolution. *Journal of Computational Physics* **103** (1), 16–42.
- LIGHTHILL, M. J. 1956 Viscosity effects in sound waves of finite amplitude. In *Surveys in Mechanics* (ed. G. K. Batchelor & R. M. Davies), pp. 250–351. Cambridge University Press.
- LIGHTHILL, M. J. 1993 Some aspects of the aeroacoustics of extreme-speed jets. In *Symposium on Aerodynamics & Aeroacoustics* (ed. K. Y. Fung), pp. 39–48.
- NICHOLS, J. W., LELE, S. K. & SPYROPOULOS, J. T. 2013 The source of crackle noise in heated supersonic jets.
- OERTEL, H. 1979 Kinematics of mach waves inside and outside supersonic jets. In *Recent Developments in Theoretical and Experimental Fluid Mechanics* (ed. U. Müller, K.G. Roesner & B. Schmidt), pp. 121–136. Springer Berlin Heidelberg.
- PANTANO, C. & SARKAR, S. 2002 A study of compressibility effects in the high-speed turbulent shear layer using direct simulation. *Journal of Fluid Mechanics* **451**, 329–371.
- PESTORIUS, F. M. & BLACKSTOCK, D. T. 1974 Propagation of finite amplitude noise. In *Proceedings of Copenhagen Symposium on Finite Amplitude Effects in Fluids*.
- PETITJEAN, B. P. & McLAUGHLIN, D. K. 2003 Experiments on the nonlinear propagation of noise from supersonic jets.
- PETITJEAN, B. P., VISWANATHAN, K. & McLAUGHLIN, D. K. 2005 Acoustic pressure waveforms measured in high speed jet noise experiencing nonlinear propagation. pp. 1371–1382.
- PHILLIPS, O. M. 1960 On the generation of sound by supersonic turbulent shear layers. *Journal of Fluid Mechanics* **9**, 1–28.
- PRESS, W. H., FLANNERY, B. P., TEUKOLSKY, S. A. & VETTERLING, W. T. 1986 *Numerical Recipes*. Cambridge University Press.
- SANDHAM, N. D. 1989 A numerical investigation of the compressible mixing layer. PhD thesis, Stanford University.
- SANDHAM, N. D. & REYNOLDS, W. C. 1990 Compressible mixing layer - linear theory and direct simulation. *AIAA Journal* **28** (4), 618–624.
- SARKAR, S. 1992 The pressure-dilatation correlation in compressible flows. *Physics of Fluids A* **4** (12), 2674–2682.
- SZEWCZYK, V. M. 1978 The role of flow acoustic interaction in jet noise studies. PhD thesis, University of Southampton.
- TAM, C. K. W. & WEBB, J. C. 1993 Dispersion-relation-preserving finite difference schemes for computational acoustics. *Journal of Computational Physics* **107** (2), 262–281.
- THOMPSON, K. W. 1987 Time dependent boundary conditions for hyperbolic systems. *Journal of Computational Physics* **68** (1), 1–24.

1.

1. Report Type

Final Report

Primary Contact E-mail**Contact email if there is a problem with the report.**

jbfreund@illinois.edu

Primary Contact Phone Number**Contact phone number if there is a problem with the report**

2177627609

Organization / Institution name

University of Illinois at Urbana-Champaign

Grant/Contract Title**The full title of the funded effort.**

JET CRACKLE

Grant/Contract Number**AFOSR assigned control number. It must begin with "FA9550" or "F49620" or "FA2386".**

FA9550-10-1-0432

Principal Investigator Name**The full name of the principal investigator on the grant or contract.**

Jonathan Freund

Program Manager**The AFOSR Program Manager currently assigned to the award**

PONNAPPAN

Reporting Period Start Date

8/15/2010

Reporting Period End Date

2/14/2015

Abstract

Fighter jets and other aircraft with high specific thrust engines can make a particularly intense type of noise that has come to be called crackle. Its rough, sporadic character is sometimes likened to super-loud paper tearing or the sharp staccato of water drops added to hot oil. It is unmistakably different than lower speed jet noise. Its frequency content, extreme intensity, and sporadic character make it particularly annoying and potentially injurious to insufficiently protected hearing. Observations suggest that it consists of series of intense shock-like sound waves, which arrive intermittently in groups. Between these shock groups a less intense but still loud standard jet noise is heard. The steepened shock-like character is suggestive of nonlinear development, but to what degree they attain this character at generation versus nonlinear steepening during propagation is unclear. There is evidence that both are key factors in crackle. It is also unclear whether the intermittency of crackle is due to the changing character of the turbulence or if it is a stochastic propagation effect.

We have complete a set of detailed direct numerical simulations of free shear flows to investigate turbulence as a source of jet crackle. This report includes (1) detailed documentation of these simulations, (2) their verification and

validation, (3) and several post-processing investigation the underlying mechanics of jet crackle, including detailed quantification of the near acoustic field, analysis of statistical metrics of jet crackle, analysis of sound-field nonlinear effects, and the relation of crackle to the linear instability modes supported by free shear flows. This is the first-ever such detailed investigation of these mechanisms. It has revealed mechanisms that can potential be harnessed to suppress this type of noise.

Distribution Statement

This is block 12 on the SF298 form.

Distribution A - Approved for Public Release

Explanation for Distribution Statement

If this is not approved for public release, please provide a short explanation. E.g., contains proprietary information.

SF298 Form

Please attach your SF298 form. A blank SF298 can be found [here](#). Please do not password protect or secure the PDF
The maximum file size for an SF298 is 50MB.

[edit_this_front_matter.pdf](#)

Upload the Report Document. File must be a PDF. Please do not password protect or secure the PDF . The maximum file size for the Report Document is 50MB.

[final_report.pdf](#)

Upload a Report Document, if any. The maximum file size for the Report Document is 50MB.

Archival Publications (published) during reporting period:

Changes in research objectives (if any):

Change in AFOSR Program Manager, if any:

Extensions granted or milestones slipped, if any:

AFOSR LRIR Number

LRIR Title

Reporting Period

Laboratory Task Manager

Program Officer

Research Objectives

Technical Summary

Funding Summary by Cost Category (by FY, \$K)

	Starting FY	FY+1	FY+2
Salary			
Equipment/Facilities			
Supplies			
Total			

Report Document

Report Document - Text Analysis

Report Document - Text Analysis

Appendix Documents

2. Thank You

E-mail user

Jun 09, 2015 20:52:05 Success: Email Sent to: jbfreund@illinois.edu